Computational Fluid Dynamics Based Mixing Prediction for Tilt Pad Journal Bearing TEHD Modeling—Part II: Implementation With Machine Learning

Jongin Yang
Mem. ASME
Department of Mechanical Engineering,
Texas A&M University,
College Station, TX 77840
e-mail: jiyang@tamu.edu

Alan Palazzolo
Fellow ASME
Department of Mechanical Engineering,
Texas A&M University,
College Station, TX 77840
e-mail: a-palazzolo@tamu.edu

Reynolds based thermo-elasto-hydrodynamic (TEHD) simulations of tilting pad journal bearings (TPJBs) generally provide accurate results; however, the uncertainty of the pad's leading edge thermal boundary conditions causes uncertainty of the results. The highly complex thermal-flow mixing action between pads (BPs) results from the oil supply nozzle jets and geometric features. The conventional Reynolds approach employs mixing coefficients (MCs), estimated from experience, to approximate a uniform inlet temperature for each pad. Part I utilized complex computational fluid dynamics (CFD) flow modeling to illustrate that temperature distributions at the pad inlets may deviate strongly from being uniform. The present work retains the uniform MC model but obtains the MC from detailed three-dimensional CFD modeling and machine learning, which could be extended to the radially and axially varying MC case. The steps for implementing an artificial neural network (ANN) approach for MC regression are provided as follows: (1) utilize a design of experiment step for obtaining an adaptable training set, (2) conduct CFD simulations on the BP to obtain the outputs of the training set, (3) apply an ANN learning process by Levenverg–Mardquart backpropagation with the Bayesian regularization, and (4) couple the ANN MC results with conventional TEHD Reynolds models. An approximate log fitting method provides a simplified approach for MC regression. The effectiveness of the Reynolds TEHD TPJB model with ANN regression-based MC distributions is confirmed by comparison with CFD based TEHD TPJB model results. The method obtains an accuracy nearly the same as the complete CFD model, but with the computational economy of a Reynolds approach. [DOI: 10.1115/1.4047751]

Keywords: bearing design and technology, fluid film lubrication, hydrodynamic lubrication, journal bearings, thermoelastohydrodynamic lubrication

1 Introduction

Multiphysics theories for tilting pad journal bearing (TPJB) modeling have been investigated during the past six decades, as discussed in Part I. As part of that effort a highly approximate mixing theory was developed to quantify the effects of the thermal phenomena between pads (BPs) on the pad inlet temperature. The limitations of the mixing theory in the Reynolds model were discussed in Refs. [1–5]. Yang and Palazzolo [4,5] presented an alternative approach employing computational fluid dynamics (CFD) thermal-flow modeling throughout the TPJB, including the particular BP regions. Their approach is validated in Part I by comparison with test results from the literature. Although highly accurate, the practicality of using the CFD TPJB approach in a design setting is constrained by its large computation time requirements. Therefore, this paper develops a means to improve the accuracy of the computationally quicker Reynolds modeling approach, utilizing improvements in pad inlet temperature prediction, derived from CFD modeling of a large set of representative TPJBs.

Table 1 contains a shortlist of mixing theory developments. The non-dimensional parameter Ya is newly defined in this study and is the ratio of the BP inflow and outflow (Q_{in}/Q_{out}). It will be shown that Ya is the dominant parameter influencing the mixing coefficient (MC), and previous MC methods can be expressed in terms of Ya. Ettles [6] introduced the first form of the MC (constant MC) and compared it to published results for thrust bearings. As shown in Fig. 1, the MC was constant over the entire Ya range, and it has a large uncertainty (MC 0.4–1.0). Mitsui et al. [8] improved the MC prediction (upstream MC) with a mass and heat balance approach defining the MC on the upstream flow. However, substantial errors may still occur (MC >1, Fig. 1). Pinkus [23] presented an approach (upstream MC) identical to Mitsui et al. [8] by applying the MC on the upstream flow.

Suh and Palazzolo's [19] hybrid MC method combined the constant MC and upstream MC methods to overcome a weakness encountered in Mitsui et al. [8]. The method still contains considerable uncertainty (MC 0.4–1.0). The present approach uses a log fitting method versus Ya to obtain a more accurate MC, ranging continuously in (MC 0.4–1.0). The basis of the approach lies primarily in matching the Reynolds and CFD approach results, utilizing CFD as a high accuracy benchmark for the Reynolds model. Thousands of CFD simulations were performed in developing the log fitting method, as indicated in Fig. 1. The log fitting method can be easily

---

Contributed by the Tribology Division of ASME for publication in the Journal of Tribology. Manuscript received August 9, 2019; final manuscript received June 22, 2020; published online August 3, 2020. Assoc. Editor: Daejong Kim.

Table 1 Previous and proposed MC methods

Researchers	Method	$\overline{\mathrm{MC}}(\|Ya\|)$	References
Ettles [6]	Constant MC	MC_K	[7]
Mitsui et al. [8]	Upstream MC	$\mathrm{MC}_K\|Ya\|$	[9–18]
Suh and Palazzolo [19]	Hybrid MC	$\min\,[\|Ya\|, \mathrm{MC}_K]$	[20–22]
(♣) Present	Log MC	$\min\,[\mathrm{MC}_{K1}\ln(\|Ya\|) + \mathrm{MC}_{K2}, 1]$	–
(♣) Present	ANN MC	–	–

Note: MC_K is an empirically assumed MC value.

incorporated into Reynolds based TPJB software for solving practical problems. A second approach for obtaining MC utilizes an artificial neural network (ANN) for further accuracy improvement.

Researchers [1–3] have developed non-MC based predictions for pad leading edge temperatures by considering detailed BP flows. Hagemann and Schwarze [2,3] proposed a simplified BP model composed of a circular arc with effective thermal boundary conditions located at the radius of the shaft, such as an effective supply temperature, mean upper BP temperature, and eddy conductivity. Only the fluid film domain for the lowest BP is modeled, and it is coupled to the adjoining pad film domains. Thus, the pad temperature boundary condition at the pad leading and trailing edges is not required since the modeling domain includes the BP and the pad film domains for the pads that bound the BP.

However, temperatures along the upper surface boundary of the BP domain must be prescribed as an effective supply temperature. Also, the upper BP boundary condition is dependent on whether the flow is supplied or discharged. This method makes calculations somewhat complicated due to dependence of the upper boundary condition on the flow direction, and to the many approximate assumptions. It is also difficult to accurately model the three-dimensional (3D) flow characteristics due to the neglect of the thermal coupling of all BPs.

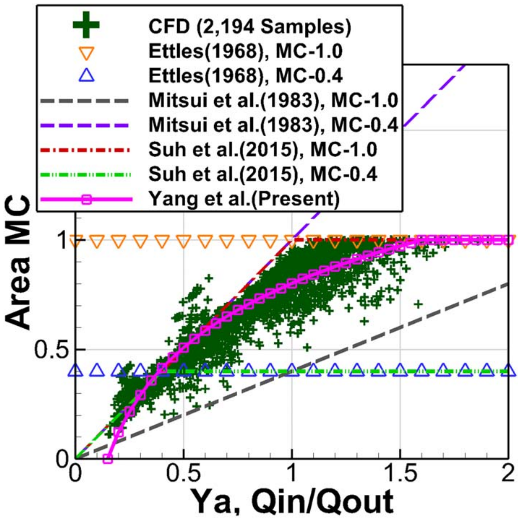

Fig. 1 Comparison of previous MC methods

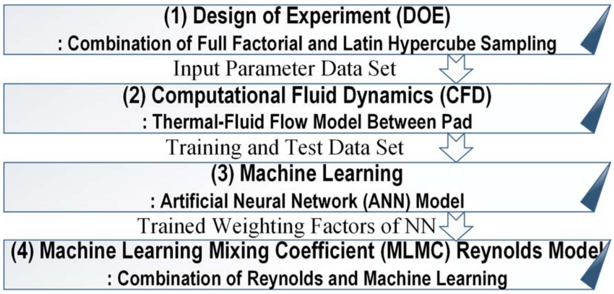

Fig. 2 Overview of the MLMC Reynolds process

Abdollahi and San Andrés [1] considered two flow conditions between pads with the assumptions that the portion of hot oil with supply oil (a) is discharged into side outlets (no recirculation flow) or (b) recirculates between pads (no side leakage flow). For calculating the pad inlet temperature, they applied a heat balance on each condition for the BP, with a newly defined mixing efficiency parameter. Two unknown side leakage and recirculating temperatures are needed for each heat balance in order to consider such flow conditions. The unknown temperatures are obtained from a heat balance on the upper BP. References [1,2] utilize a bulk flow model, which does not include complex 3D thermal-flow effects. Their approach also defines other uncertain parameters like mixing efficiency parameter, side leakage temperature, and recirculating temperature which may vary according to the flow regime, film thickness, bearing geometry, and operating condition.

In comparison, the present study shows that the MC is highly and in some cases non-linearally, dependent on various operating and geometry parameters. Therefore, the MC prediction model has to include these parameters and be derived by solving the Navier–Stokes equations, including the fully 3D mixing phenomena between pads. Artificial intelligence (AI) provides a highly reliable means for accurate prediction of pad inlet temperature, based on large dimensional training sets obtained from the CFD solutions and design of experiments (DOEs). The ANN machine learning technique has robust capability independent of the degree of nonlinearity considered [24,25]. AI machine learning's increasing popularity is due to the rapid development of computational resources, improved algorithms, and widespread applications. AI has recently been applied in the optimization of plasmonic thin-film organic solar cells [25], stock market price prediction [26], urban growth [27], response prediction of large buildings [28], pavement structural evaluation [29], breast cancer type prediction [30], analysis of water quality in estuaries [31], etc.

The main contribution of this study is an advanced mixing temperature prediction method that utilizes ANN trained from large databases of CFD results. A DOE method is proposed, which is tailored for MC prediction. The Levenverg–Mardquart backpropagation (LMB) [32–34] algorithm with Bayesian regularization [35] is employed for training the ANN. Finally, the ANN-based method is combined with the conventional Reynolds model to obtain the machine learning mixing coefficient (MLMC) Reynolds model. Its accuracy is verified by comparing it with the full thermo-elasto-hydrodynamic (TEHD)-CFD model developed in Part I.

2 Overview of the MLMC Reynolds Model

Figure 2 shows a flow diagram of the MLMC Reynolds, TPJB modeling approach. Here, machine learning acts as a regression model for MC prediction between pads, within practical ranges of selected input parameters. ANN is utilized, and its artificial neurons are trained to search for adaptable weighting. LMB with Bayesian regularization is implemented in an in-house code and

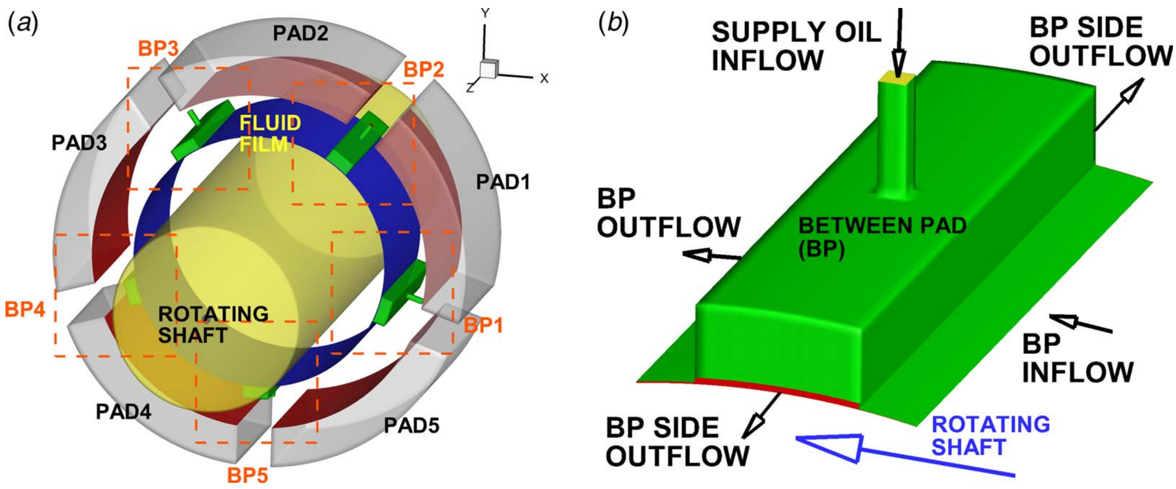

Fig. 3 BP configuration of the TPJB: (*a*) full domain and (*b*) trained BP region

is applied to train the ANN from the training and test data sets generated in the CFD model. The DOE step combines full factorial and Latin hypercube sampling (LHS) [36,37] to produce a suitable input design space for the regression. Several thousand cases from the input design space are simulated using 3D CFD models for BP MC prediction. The model geometry and meshing are automatically updated for different input parameter cases. This performed with a PYTHON-based code (Job Script) in the CFD model, to improve computational efficiency. Furthermore, the full input parameter domain is divided into several tens of calculation nodes for parallel computation, using the computational resources of the Texas A&M High-Performance Research Computing Center (HPRC).

Figure 3(*a*) illustrates the rotor-bearing system, and Fig. 3(*b*) illustrates the BP region. The CFD model's primary focus is on the BP region for generating training and test data sets for obtaining ANN predicted MC for each BP. The DOE method is implemented by the MATLAB DOE functions. The commercial CFD code (CFX) is used to maintain consistency with the verified full CFD model of the TPJB rotor-bearing system in Part I. The trained ANN provides the MC and other outputs and is embedded in the Reynolds model solver. The ANN acts as a sub-function with the BP geometric parameter and operating condition as inputs, and MC, shear stress, pressure drop, and supply oil flowrate as outputs. The MCs from the ANN are iteratively calculated in the transient solver of the MLMC Reynolds model during the computation, with additional details described in Sec. 6.

3 Design of Experiment

The DOE step forms the design space, which is crucial for robust performance of the regression model. The design space implies the space within the range of the input parameters, and the design points indicate each input parameter data set. Full factorial with three-level factors, as shown in Fig. 4(*a*), provides globally uniform design points which facilitates accurate regression. However, this requires a massive amount of design points according to the increase of the factors (input parameter number). For example, it needs 3^n design points for n factors, i.e., it requires 19,683 design points for nine factors, which is the number of input parameters utilized in this research for the MC prediction. Thus, it is computationally burdensome to apply the three-level full factorial approach to large input parameter sets, when considering the CFD computation time.

An alternative approach with far fewer design points is a simple two-level full factorial model, as illustrated in Fig. 4(*b*). However, it has a reduced accuracy region near the middle of the full design space, and a reduced capacity for capturing non-linear dependence of the MC on input parameters. Thus, a DOE combination methodology of the two-level full factorial and the LHS with minimax space filling design is proposed. The reason for not employing solely LHS is because, by itself, it can have poor accuracy near the outer surface. The LHS approach generates design points randomly and uniformly over the full design space, and the design point number of the LHS is specified to be identical with that of the two-level full factorial. This method can overcome the pitfall of the conventional approach and reduce the number of design points relative to three-level full factorial. For instance, 1024 design points are enough for the nine input parameters when using the proposed method, while the full factorial requires 19,683 design points. Figure 4(*c*) shows the design space which is produced by the combination DOE of the two-level full factorial and LHS. The advantage of the combination DOE method is demonstrated in Sec. 7.2, and the case of the two-level full factorial, and two times LHS of the number of the full factorial in Fig. 4(*d*), is also investigated in Sec. 7.2.

4 Computational Fluid Dynamics Modeling for "Between Pads" Thermal-Flow

Mixing coefficients relate the pad inlet (BP outlet) temperature to the supply oil temperature and the outlet (BP inlet) temperature of the previous pad. For the present analysis, define the "area MC" as

$$\overline{\mathrm{MC}} \equiv \frac{\overline{T}_{out} - T_{sup}}{\overline{T}_{in} - T_{sup}} \tag{1}$$

where the mass flow weighted, area averaged temperature is defined as

$$\overline{T} = \frac{\iint \rho u c_p T dA}{\iint \rho u c_p dA} \tag{2}$$

for both $\overline{T}_{out}$ and $\overline{T}_{in}$. Likewise define the axially varying, or simply "axial MC" as

$$\mathrm{MC}(z) \equiv \frac{\widehat{T}_{out}(z) - T_{sup}}{\widehat{T}_{in}(z) - T_{sup}} \tag{3}$$

where the mass flow weighted, radial averaged temperature is defined as

$$\widehat{T}(z) = \frac{\int \rho u c_p T dr}{\int \rho u c_p dr} \tag{4}$$

for both $\hat{T}_{out}$ and $\hat{T}_{in}$. The forms (1) and (3) suggest that the "area" MC and "axial" MC are in effective non-dimensional

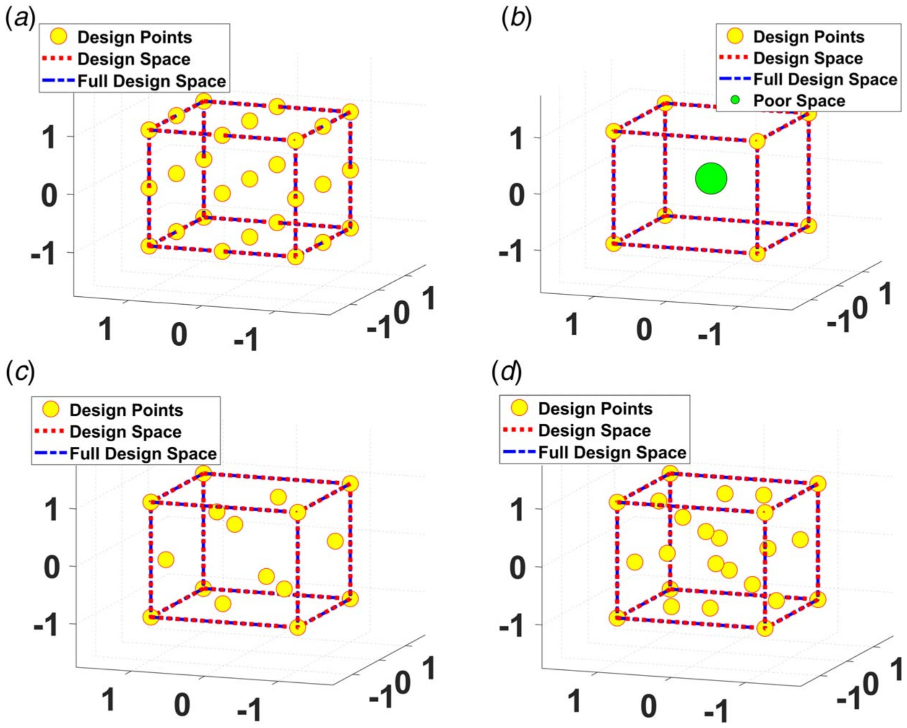

Fig. 4 Proposed DOE approach which combines full factorial and LHS: (*a*) full factorial (level 3), (*b*) full factorial (level 2), (*c*) full factorial (level 2) + LHS × 1, and (*d*) full factorial (level 2) + LHS × 2

measures of the mass flow weighted, area, and radially averaged, pad inlet (BP outlet) temperatures. These non-dimensional forms are appropriate for regression via the ANN machine learning approach.

A k–ω based shear stress transport (SST) turbulence model with a gamma transitional model, and energy equation with temperature-dependent, variable viscosity are employed to simulate the thermal-flow. A two-phase mixture model is also included for the case where cavitation occurs, with pressures below the saturation pressure of the oil.

Figure 5 shows all BP dimensions and boundary conditions. The constant supply oil total pressure is applied at face (1). The pressure at the BP inlet (3) and outflow (5) faces varies along the bearing axial direction and is well represented by

$$P_{in}(z) = \frac{3}{2}\overline{P}_{in}\left\{1 - \left(\frac{z}{L_1}\right)^2\right\} \tag{5}$$

$$P_{out}(z) = \frac{3}{2}\overline{P}_{out}\left\{1 - \left(\frac{z}{L_1}\right)^2\right\} \tag{6}$$

where the mean pressure along the bearing axial direction is defined by ($\overline{P} \equiv 1/L_1 \times \int_0^{L_1} P dz$), and where these functions are a

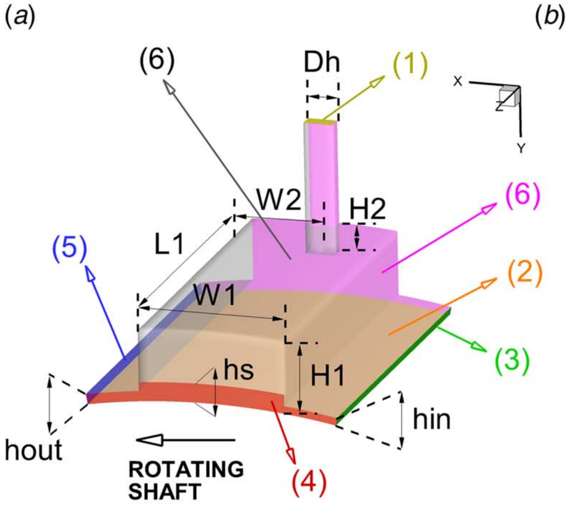

(*b*)

No.	Description	Prescribed Variables
(1)	Supply Oil flow	$P_{t,sup}$, T_{sup}
(2)	Rotating Shaft	U_s, T_w
(3)	BP Inflow	P_{in}, T_{in}
(4)	BP Side Outflow	P_{amb}
(5)	BP Outflow	P_{out}
(6)	Outer Wall	h_{amb}, T_{amb}
(7)	Symmetric	-

Fig. 5 BP dimensions and boundary conditions

Table 2 List of all input parameters $P_{(i)}$ for the BP region

No.	Parameters	No.	Parameters
$P_{(1)}$	W_1	$P_{(10)}$	T_{sup}
$P_{(2)}$	$W_2/(W_1 - D_h)$	$P_{(11)}$	$T_{in} - T_w$
$P_{(3)}$	L_1/R_s	$P_{(12)}$	U_s
$P_{(4)}$	H_1/t_p	$P_{(13)}$	$P_{t,sup}$
$P_{(5)}$	D_h/W_1	$P_{(14)}$	$\overline{P}_{in}$
$P_{(6)}$	R_s	$P_{(15)}$	$\overline{P}_{out}$
$P_{(7)}$	h_s/R_s	$P_{(16)}$	$h_{in}/C_{l,b}$
$P_{(8)}$	H_2/H_1	$P_{(17)}$	$h_{out}/C_{l,b}$
$P_{(9)}$	T_{in}	$P_{(18)}$	μ_f

maximum at the symmetric face (6). The pressure at the BP side outflow face (4) is held at ambient. The average pressures $\overline{P}_{in}$ and $\overline{P}_{out}$ in Eqs. (5) and (6) are used as input parameters (design points) of the machine learning, and the profiles in the equations are prescribed in the CFD.

For the turbulence governing equations, a zero gradient condition is applied at the faces (1), (3), (4), and (5). For the energy equation's boundary condition, faces (1), (2), and (3) are prescribed with the temperature 30 °C and the heat convection boundary condition with 50 W/m^2. The BP outer wall (6) is prescribed with the heat transfer boundary condition (50 W/(m^2 K), 30 °C). However, the heat convection to the BP outer wall (6) is negligible because its heat transfer is much lower than the flow's advection heat.

All possible input parameters in the regression model are listed in Table 2, and are based on the BP dimensions and boundary conditions in Fig. 5. Some parameters are non-dimensionalized to maintain similarity according to a change of journal radius. The standard pad thickness t_p is defined by $0.25R_s$, and the standard radial bearing clearance is also defined as $C_{l,b} = (0.0749/50.8)R_s$, where R_s is the journal radius, and μ_f is the dynamic viscosity of the lubricant. The term U_s is the surface velocity of the shaft.

A grid test was carried out with the parameters in Table 3 to check for grid independence before the CFD training set computation. A mesh of 27,675 elements (0.75 mm element size) shows sufficient grid independence and is applied for producing training and test data sets. This was based on prediction of the MC and the static supply pressure.

Figure 6 shows the calculation process in CFD for creating the training and test data sets. The proposed DOE creates the training data set, and the test data set is made with randomly extracted input parameters. The computation is performed after distributing the total input parameter set into several tens of calculation nodes (N_c) for obtaining results within a realistic time limit. Each Job script controls all computation sequences, including updating the input parameter set, generating geometry and meshing, and solving the governing equations of the BP physics. This process repeats until each calculation node completes its assigned input data set (N_i), while building the result (outputs) files, including MC, shear stress, and pressure data.

Table 3 BP input parameters (Table 2) values for the grid test

Parameter no. i	Values	Unit	Parameter no. i	Values	Unit
$P_{(1)}$	12	(deg)	$P_{(10)}$	45	(C)
$P_{(2)}$	0.5	–	$P_{(11)}$	0	(C)
$P_{(3)}$	0.5	–	$P_{(12)}$	60	(m/s)
$P_{(4)}$	0.41	–	$P_{(13)}$	0.5	(MPa)
$P_{(5)}$	0.21	–	$P_{(14)}$	0.25	(MPa)
$P_{(6)}$	50.8	(mm)	$P_{(15)}$	0.25	(MPa)
$P_{(7)}$	0.0084	–	$P_{(16)}$	1.0	–
$P_{(8)}$	0.3	–	$P_{(17)}$	1.5	–
$P_{(9)}$	80	(C)	$P_{(18)}$	ISO32	–

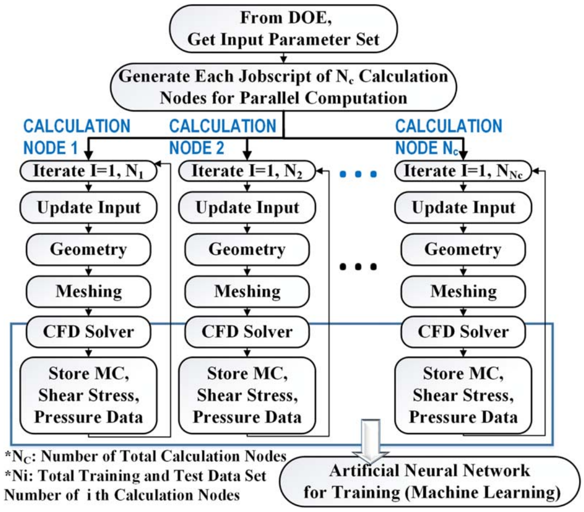

Fig. 6 Calculation process for CFD BP modeling of training set from DOE

5 Machine Learning (Artificial Neural Network)

5.1 Levenberg–Marquardt Backpropagation Algorithm With Bayesian Regularization. The data set utilized in the training process is referred to as the "training data set." The critical part for successful machine learning is to show consistent performance no matter which training data set is utilized. The process of accomplishing consistent performance is called generalization. The most common reason for generalization failure is overfitting. Various techniques have been developed to prevent the overfitting problem. The Bayesian regularization [35] techniques were adopted in this research. The test data set is used to check whether overfitting occurs during the training process (cross validation), and does not participate in the training process. It is merely used to check the ANN performance with the training data set.

Figure 7 illustrates the overall ANN and highlighted connections for neuron j. The ANN consists of an input layer, a hidden layer, and an output layer. One hidden layer is contemplated. The calculation process is divided into the forward and backward propagation, as shown in Figs. 7(*a*) and 7(*b*), respectively. In the forward propagation process, the neuron's net value X_j^k, output Y_j^k, and slope S_j^k are stored, and then, the defined delta $\delta_{o,j}^k$ is obtained in the backward propagation process. Throughout this process, the Jacobian matrix is computed, and the LMB algorithm with the Bayesian regularization is applied using the Jacobian matrix, during the iterative learning process.

The relation of the input and output for neuron j can be written as

$$X_j^k = \sum_{i=1}^{n_i} w_{j,i}^k y_{j,i}^k + w_{j,0}^k \tag{7}$$

$$Y_j^k = \tanh\left(X_j^k\right) \tag{8}$$

where $w_{j,i}^k$ and $y_{j,i}^k$ are the weighting factor and neuron input value, respectively (i: input index of a neuron from 0 to n_i, j: neuron index from 1 to n_j, and k: layer index from 1 to 2), and the $w_{j,0}^k$ is the bias weighting factor. The hyperbolic tangent in Eq. (8) is considered as an activation function of the neuron. The X_j^k is the neuron's net value, and the Y_j^k is the neuron's output.

Regularization is the learning technique for the ANN to be generalized adaptably by minimizing the weighting factors, and Bayesian regularization [35] is applied for this purpose. The cost function (objective function), which represents the ANN

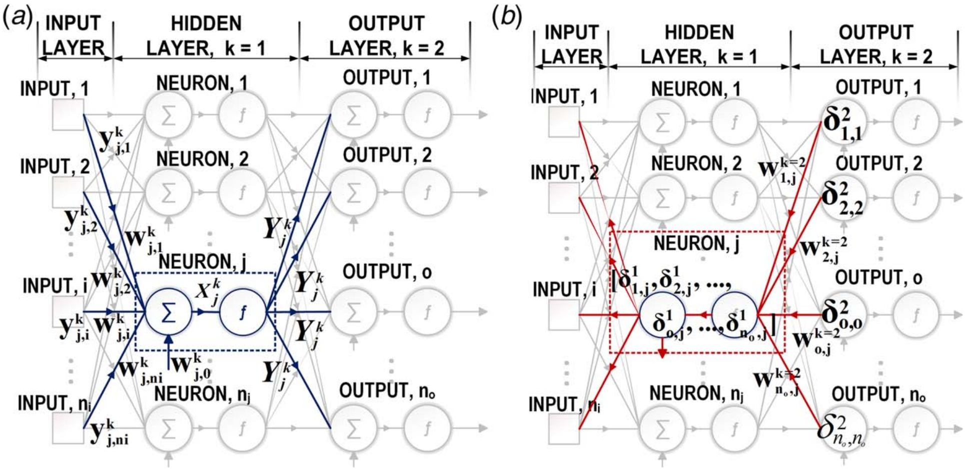

Fig. 7 ANN connection for neuron *j*: (*a*) forward propagation and (*b*) backward propagation

performance, is defined as

$$F_{cost} = \beta \times \mathrm{SSE} + \alpha \times \mathrm{SSW} \tag{9}$$

$$\mathrm{SSE} = \{e\}^T\{e\} \tag{10}$$

$$\mathrm{SSW} = \{w\}^T\{w\} \tag{11}$$

$$\{e\} = [e_1|_{p=1}, \ldots, e_{n_o}|_{p=1}, \ldots, e_1|_{p=n_p}, \ldots, e_{n_o}|_{p=n_p}]^T, \ (n_o \times n_p) \times 1 \tag{12}$$

$$\begin{aligned}\{w\} = [&w^1_{1,0}, w^1_{1,1}, \ldots, w^1_{1,n_i}, \ldots, w^1_{n_j,0}, w^1_{n_j,1}, \ldots, w^1_{n_j,n_i},\\ &w^2_{1,0}, w^2_{1,1}, \ldots, w^2_{1,n_j}, \ldots, w^2_{n_o,0}, w^2_{n_o,1}, \ldots, w^2_{n_o,n_j}]^T\end{aligned} \tag{13}$$

The term sum of squared weighting (SSW) factors in Eq. (11) is added to the sum of squared errors (SSE) in Eq. (10), and the regulation parameters α and β are introduced. The error and weight vectors are given in Eqs. (12) and (13), respectively. The p is the index of the training data set from 1 to n_p. The weighting factor ($w^k_{j,i}$) and bias factor ($w^k_{j,0}$) are utilized as the ANN's activation function parameters as in Eqs. (7) and (8), and it is determined from the training process. The optimal α and β in Eq. (9) are obtained from Ref. [35], as

$$\alpha = \frac{\gamma}{2\mathrm{SSW}} \tag{14}$$

$$\beta = \frac{N_T - \gamma}{2\mathrm{SSE}} \tag{15}$$

where N_T is the total number of training data set ($n_o \times n_p$), and it is utilized in Eq. (15), ($n_o \times n_p$) indicates the total number of training data sets, where the number of training sets is (n_p), and the number of outputs is (n_o). For instance, the number of training data set (n_p) is 1536, and all outputs have $n_o = 1$ for the area-MC ANN. The regularization parameters adjust the errors and weighting factors during the training process. For instance, the training process is performed to focus on reducing the errors if $\alpha \gg \beta$ and on decreasing the weighting factors if $\beta \ll \alpha$. The effective parameter γ is obtained from

$$\gamma = N_W - 2\alpha \times trace([H]^{-1}) \tag{16}$$

$$[H] \simeq 2\beta[J]^T[J] + 2\alpha[I] \tag{17}$$

where N_W is the total number of weighting factors ($n_i \times n_j + n_j + n_j \times n_o + n_o$). From the Gauss–Newton approximation, the Hessian matrix $[H]$ can be expressed by Eq. (17) [35]. The gradient vector of the objective function can be written by

$$\{g\} = 2\beta[J]^T\{e\} + 2\alpha\{w\} \tag{18}$$

$$\{w\} = \{w*\} - (2\beta[J^*]^T[J^*] + 2(\alpha+\mu)[I])^{-1}\{g*\} \tag{19}$$

The combination coefficient μ is a parameter applied in the learning process, which is not needed to provide a specific value, and will be discussed further in Sec. 5.2.

The Hessian matrix $[H]$ and gradient vector $\{g\}$ are used to update the weight factor vector $\{w\}$ by the relation in Eq. (19), where the superscript * means present iteration step. Equation (19) represents the update rule of the LMB with the regularization parameters.

The major role of the LMB is to determine the Jacobian matrix $[J]$. The Jacobian matrix consists of the derivative of the weighting factors with regard to the output errors. The error is defined by $OUTC_o - OUTN_o$, which is the difference of the desired output value ($OUTC_o$) and ANN output value ($OUTN_o$), where o is the output neuron index, from 1 to n_o. The desired output value is obtained from the CFD simulation. The structure of the entire Jacobian matrix is organized with the hidden layer column and the output layer column for each training data set row. This insures that the matrix order corresponds with that of the defined error $\{e\}$ and weight vector $\{w\}$

$$[J] = \left[\begin{array}{c:c:c} \begin{gathered}hidden\\ layer\downarrow\end{gathered} & \begin{gathered}output\\ layer\downarrow\end{gathered} & \\ \hdashline \boldsymbol{J}_{hid,1} & \boldsymbol{J}_{out,1} & \leftarrow training\,set,1 \\ \hdashline \boldsymbol{J}_{hid,2} & \boldsymbol{J}_{out,2} & \leftarrow training\,set,2 \\ \hdashline \vdots & \vdots & \vdots \\ \hdashline \underset{n_o\times(n_i\times n_j+n_j)}{\underline{\boldsymbol{J}_{hid,p}}} & \underset{n_o\times(n_j\times n_o+n_o)}{\underline{\boldsymbol{J}_{out,p}}} & \leftarrow training\ set,\,p \\ \hdashline \vdots & \vdots & \vdots \\ \hdashline \boldsymbol{J}_{hid,n_p} & \boldsymbol{J}_{out,n_p} & \leftarrow Training\ set,\,n_p \end{array}\right] \tag{20}$$

The matrix component's ordering of the $[J_{hidp}]$ and $[J_{outp}]$ for the pth training data set are given by

$$[J_{hidp}] = \left[\begin{array}{cccccccc} \multicolumn{3}{c}{|\leftarrow \text{neuron, } 1 \rightarrow|} & \cdots & \multicolumn{3}{c}{|\leftarrow \text{neuron, } n_j \rightarrow|} & \\ \left.\frac{\partial e_1}{\partial w^1_{1,0}}\right|_p & \cdots & \left.\frac{\partial e_1}{\partial w^1_{1,n_i}}\right|_p & & \left.\frac{\partial e_1}{\partial w^1_{n_j,0}}\right|_p & \cdots & \left.\frac{\partial e_1}{\partial w^1_{n_j,n_i}}\right|_p & \begin{array}{l}\leftarrow NN \\ \text{output, } 1\end{array} \\ \vdots & \ddots & \vdots & \cdots & \vdots & \ddots & \vdots & \vdots \\ \left.\frac{\partial e_{n_o}}{\partial w^1_{1,0}}\right|_p & \cdots & \left.\frac{\partial e_{n_o}}{\partial w^1_{1,n_i}}\right|_p & & \left.\frac{\partial e_{n_o}}{\partial w^1_{n_j,0}}\right|_p & \cdots & \left.\frac{\partial e_{n_o}}{\partial w^1_{n_j,n_i}}\right|_p & \begin{array}{l}\leftarrow NN \\ \text{output, } n_o\end{array} \end{array}\right] \tag{21}$$

$$[J_{outp}] = \left[\begin{array}{cccccccc} \multicolumn{3}{c}{|\leftarrow \text{neuron, } 1 \rightarrow|} & \cdots & \multicolumn{3}{c}{|\leftarrow \text{neuron, } n_o \rightarrow|} & \\ \left.\frac{\partial e_1}{\partial w^2_{1,0}}\right|_p & \cdots & \left.\frac{\partial e_1}{\partial w^2_{1,n_j}}\right|_p & & \left.\frac{\partial e_1}{\partial w^2_{n_o,0}}\right|_p & \cdots & \left.\frac{\partial e_1}{\partial w^2_{n_o,n_j}}\right|_p & \begin{array}{l}\leftarrow NN \\ \text{output, } 1\end{array} \\ \vdots & \ddots & \vdots & \cdots & \vdots & \ddots & \vdots & \vdots \\ \left.\frac{\partial e_{n_o}}{\partial w^2_{1,0}}\right|_p & \cdots & \left.\frac{\partial e_{n_o}}{\partial w^2_{1,n_j}}\right|_p & & \left.\frac{\partial e_{n_o}}{\partial w^2_{n_o,0}}\right|_p & \cdots & \left.\frac{\partial e_{n_o}}{\partial w^2_{n_o,n_j}}\right|_p & \begin{array}{l}\leftarrow NN \\ \text{output, } n_o\end{array} \end{array}\right] \tag{22}$$

Each component of the Jacobian matrix in Eqs. (20)–(22) can be determined by the chain rule as expressed by

$$\left.\frac{\partial e_o}{\partial w^k_{j,i}}\right|_p = \left.\frac{\partial OUTC_o - OUTN_o}{\partial w^k_{j,i}}\right|_p = -\left.\frac{\partial OUTN_o}{\partial Y^k_j}\right|_p \left.\frac{\partial Y^k_j}{\partial X^k_j}\right|_p \left.\frac{\partial X^k_j}{\partial w^k_{j,i}}\right|_p \tag{23}$$

where

$$\left.\frac{\partial OUTN_{p,o}}{\partial Y^k_j}\right|_p \equiv (F^k_{o,j})'|_p \tag{24}$$

$$\left.\frac{\partial Y^k_j}{\partial X^k_j}\right|_p = (1 - Y^k_j)^2|_p \equiv S^k_j|_p \tag{25}$$

$$\left.\frac{\partial X^k_j}{\partial w^k_{j,i}}\right|_p = y^k_{j,i}|_p \tag{26}$$

The defined derivative function $(F^k_{o,j})'|_p$ and slope $S^k_j|_p$ of neuron j are represented in Eqs. (24) and (25). The multiplication of the function and slope is defined as

$$\delta^k_{o,j}|_p \equiv S^k_j|_p (F^k_{o,j})'|_p \tag{27}$$

From Eqs. (26) and (27), Eq. (23) can be rewritten as

$$\left.\frac{\partial e_o}{\partial w^k_{j,i}}\right|_p = \begin{cases} \delta^k_{o,j}|_p y^k_{j,i}|_p & \text{if } i \neq 0 \\ \delta^k_{o,j}|_p & \text{if } i = 0 \end{cases} \tag{28}$$

In Eq. (28), $y^k_{j,i}|_p$ is determined in the forward propagation process. However, $\delta^k_{o,j}|_p$ is unknown in the forward propagation process, and it is obtained in the backward propagation process, as shown in Figs. 7(*a*) and 7(*b*). The term $(F^k_{o,j})'|_p$ is the derivative of the output of the neuron j and the layer k with regard to the nonlinear function, which is made up by the activation function. Thus, $\delta^k_{o,j}|_p$ for the output layer and hidden layer can be written as

$$\delta^2_{o,j}|_p = \begin{cases} S^2_j|_p, & \text{if } o = j \\ 0, & \text{if } o \neq j \end{cases} \tag{29}$$

$$\delta^1_{o,j}|_p = w^2_{o,j}\delta^2_{o,o}|_p S^1_j|_p \tag{30}$$

5.2 Artificial Neural Network Learning Process of Levenberg–Marquardt Backpropagation-Bayesian Regularization. Figure 8 illustrates the ANN learning process for the MC regression model. The superscript * denotes the old or present value before updating the value. There are two main iteration loops of I and K. The first I iteration loop implements the identical learning processes for one hundred times. This is because the ANN performance in each learning process will be different because the procedures are performed with randomly initialized weight vectors which Nguyen and Widrow [38] presented, and it influences the ANN performance. Even though the variation in the learning process results can be minimized by the Bayesian regularization utilized in this research, a slight difference of each ANN performance still exists. Thus, the ANN with the best performance after one hundred iterations is kept for the optimal ANN MC model. The second K iteration loop represents the LMB-Bayesian regularization algorithm.

6 Description of the MLMC Reynolds Model

The ANN regression acquired from machine learning is coupled with the Reynolds model to alleviate the latter's principal shortcoming: utilizing assumed MC values for the prediction of the pad leading and trailing edge temperatures. In this study, the model will be referred to as the MLMC Reynolds model. A generalized Reynolds model is employed, including variable viscosity through the film thickness. The 3D energy equation is applied in the film and 3D structure for thermal deformation and pad flexibility effects. The specific description is provided in the earlier consecutive studies [4,19,21].

As shown in Fig. 9(*b*), there are three ANNs trained, which are area-MC, BP-pressure, and BP-drag torque and supply flowrate ANN. The vital one is the area-MC ANN, where the averaged MC (area-MC) was defined in Eqs. (1) and (2). In addition, the BP-pressure ANN is generated, which predicts pad pressure at plane (1) in Fig. 9(*a*). In Fig. 9, it is noted that the BP in and out pressure at the plane (1) is the Reynolds model's input parameters, and it is iteratively updated by the BP-pressure ANN's output. The data transfer in Fig. 9(*a*) of the staggered boundaries (planes 1 and 2) is due to the fact that the BP inlet and outlet boundaries in the CFD model are defined at the plane (2) of the Reynolds model as shown in Fig. 9(*a*). The corresponding Δx(4 deg) in the CFD is applied for the complete coupling of both Reynolds and ANN models.

Yang and Palazzolo [4] demonstrated that the contribution of the BP regions to the drag torque becomes considerable at high operating speeds. Thus, the ANN for BP-drag torque and supply flowrate

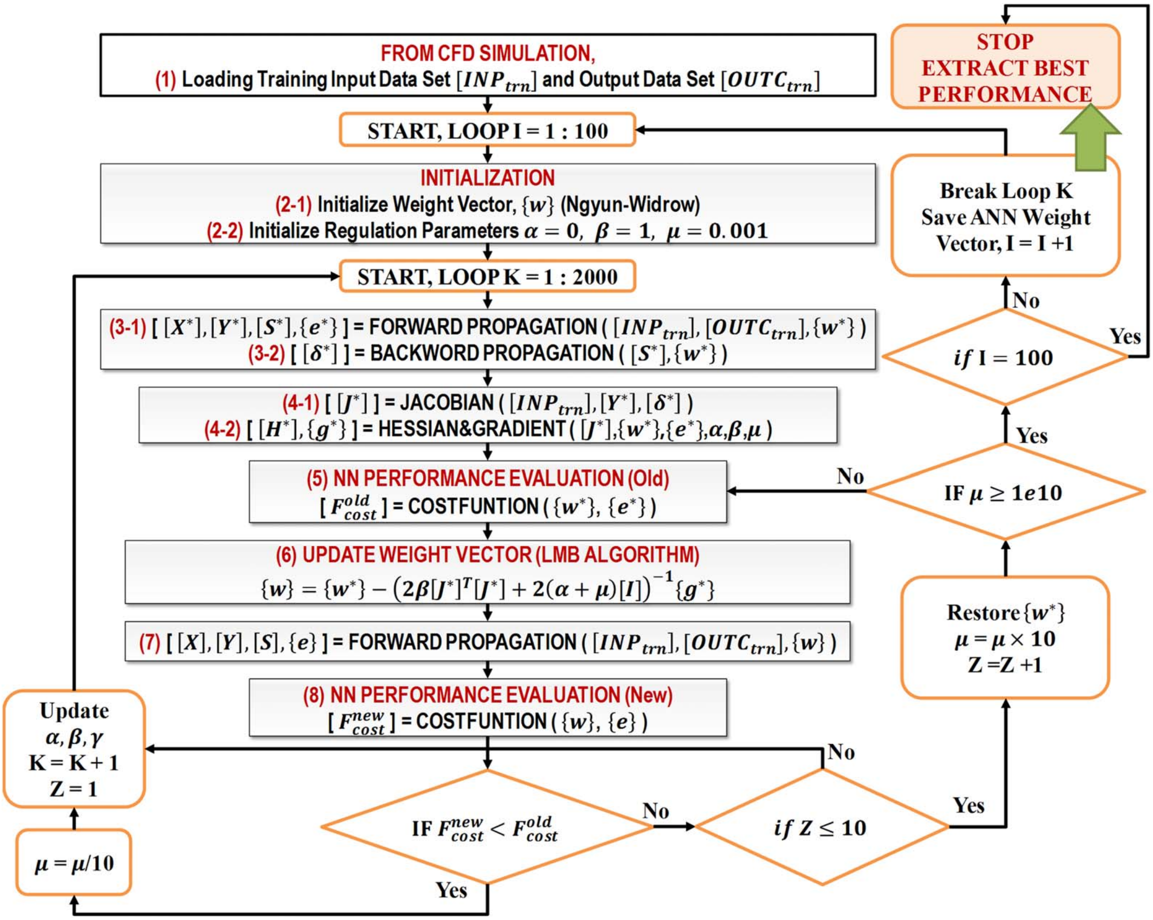

Fig. 8 ANN learning process of LMB-Bayesian regularization for good performance

is utilized to provide the drag torque contributions from the BP regions between pads, and the total supply flowrate. The drag torque between pads is summed with the drag torque on pads to obtain the total drag torque on the entire journal. The drag torque on the pads can be obtained from

$$\mathrm{DT} = \int_{A_s} \left(R_s \times \mu_f \frac{\partial u_{tng}}{\partial r} \right) dA_s \tag{31}$$

where u_{tng} is the tangential velocity at the shaft surface, μ_f is the dynamic viscosity of the lubricant, and A_s indicates the shaft area in the pad regions.

The nine input parameters in Fig. 9(*b*) were selected for having the largest influence on the MC, based on the parametric studies that are discussed in Sec. 7.1. The ANN and Reynolds models are continuously updated in the transient solver by transferring input and outputs to each other.

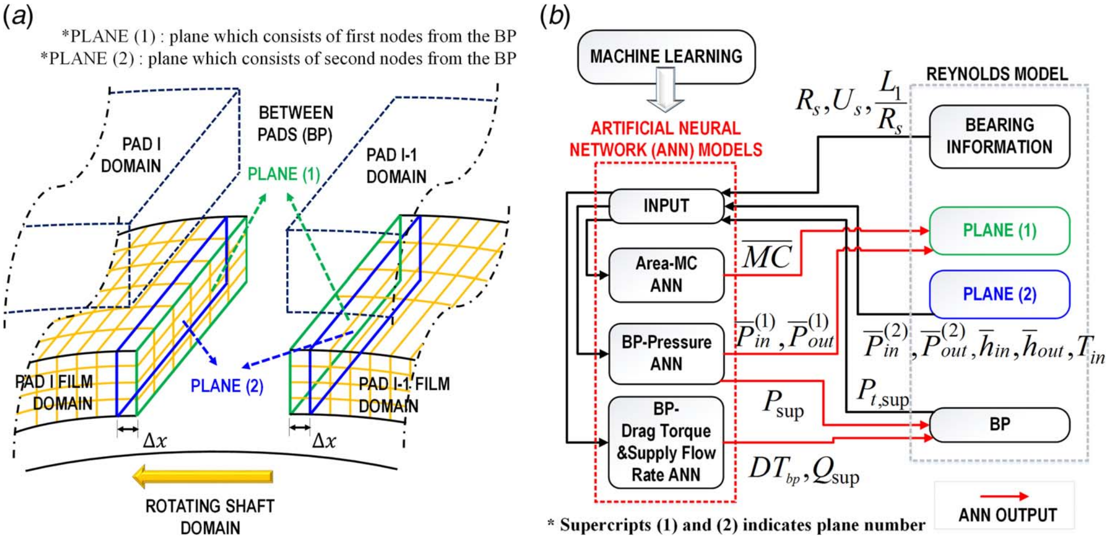

Fig. 9 Data transfer between ANN and Reynolds model: (*a*) data transfer location and (*b*) flow diagram of the data transfer between models, including drag torque, supply flowrate, pressure, MC

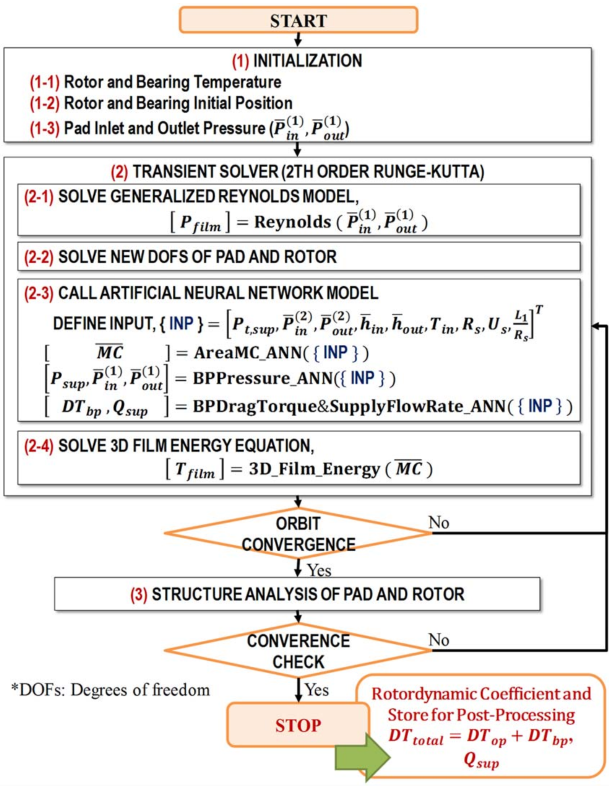

Fig. 10 Flow diagram for solution of coupled rotordynamic coefficient and MLMC Reynolds bearing model

As discussed in Part I and earlier studies [4,5], the conventional radially uniform temperature assumption in the pad inlet can cause under-prediction of shaft temperatures. This may require selection of MC outside of the conventional (0.4–1.0) range to match test or CFD results. Conversely, significant prediction errors may occur even though the MC is selected within the conventional range (0.4–1.0). To address this shortcoming of the Reynolds model, it is proposed to use the following temperature boundary condition at the shaft wall:

$$T_w = C_w \overline{T}_{film} \tag{32}$$

where $\overline{T}_{film}$ is the mean temperature of the full film domain and C_w is a correction factor that is always 1.075 and is identified in the present study. The correction factor 1.075 was estimated based on a representative CFD simulation result (9000 rpm case in Part I) and adjusted for the Reynolds model to predict the shaft temperature accurately. Finally, Fig. 10 represents the calculation procedure for the coupled rotordynamic coefficient and MLMC Reynolds bearing models.

The Reynolds 3D energy equation solution requires that all nodes in the film at the pad leading edge have prescribed temperatures. The specified temperature (BP outlet temperature) is determined by Eq. (3) and is applied to all nodes at the pad leading edge. The radially averaged BP inlet temperatures and the supply temperature are given during the calculation. The area MC is applied to the equation, and it is obtained from the area-MC ANN.

7 Results

7.1 Parameter Study of Computational Fluid Dynamics Predicted Mixing Coefficients. Table 4 lists the 18 parameters selected for describing the geometry and operating state of a BP region. Minimum, median, and maximum values were assigned to each parameter. CFD based simulations were performed changing one parameter at a time, while the remaining parameters were given their medium values, with the varied parameter assuming its minimum, median, and maximum value.

Table 4 Selected ranges of the BP input parameters $P_{(i)}$ of Table 2

Parameter[a] no.	Min, $p_{(i)}^-$	Median, $p_{(i)}$	Max, $p_{(i)}^+$	Unit
$P_{(1)}$	9	12	15	(deg)
$P_{(2)}$	0.25	0.5	0.75	–
$P_{(3)}$	0.25	0.5	0.75	–
$P_{(4)}$	0.21	0.41	0.61	–
$P_{(5)}$	0.085	0.105	0.125	–
$P_{(6)}$	25.4	50.8	76.2	(mm)
$P_{(7)}$	0.0050	0.0084	0.0118	–
$P_{(8)}$	0	0.3	0.6	–
$P_{(9)}$	60	80	100	(C)
$P_{(10)}$	40	45	50	(C)
$P_{(11)}$	−20	0	20	(C)
$P_{(12)}$	40	60	80	(m/s)
$P_{(13)}$	0.3	0.5	0.7	(MPag)
$P_{(14)}$	0	0.25	0.5	(MPag)
$P_{(15)}$	0	0.25	0.5	(MPag)
$P_{(16)}$	0.5	1.0	1.5	–
$P_{(17)}$	1.0	1.5	2.0	–
$P_{(18)}$	ISO 15	ISO 32	ISO 46	–

[a]Parameter descriptions are shown in Table 2.

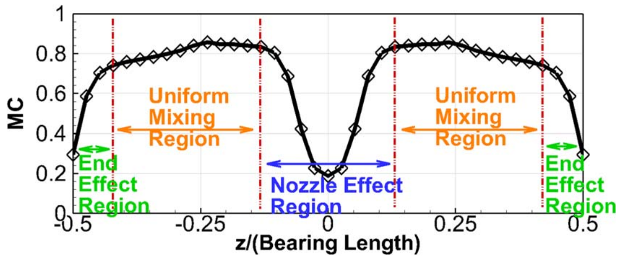

Fig. 11 Three regions representing the axial MC distribution: nozzle effect region, uniform mixing region, and the end effect region

Figure 11 shows a typical distribution of "axial" MC, by Eqs. (3) and (4), obtained from the CFD model. The axial MC distribution can be classified into three distinct regions, which are the nozzle effect region, uniform mixing region, and end effect region. Conventional mixing theory is based on the flow characteristics in the uniform mixing region, and the influence of the nozzle effect region and end effect region are treated as an extension of the uniform mixing region. However, independent consideration of the MC characteristics in the nozzle effect region and end effect region is essential, especially if the bearing is short, or direct lubrication is taken into account.

Figure 12 shows the percent changes of the area MC, by Eqs. (1) and (2), at the upper and lower bounds of the respective parameters. Table 2 shows that parameters (1)–(8) are "geometric" parameters that are fixed, and parameters (9)–(18) are "operating" parameters that may change in the iterative solution process. The geometric parameter's effects on the MC are relatively minor when compared with the operating parameter's effects. Parameters (16) $h_{in}/C_{l,b}$ and (17) $h_{out}/C_{l,b}$ show the strongest impact on the MC. It is also notable that the MC is sensitive to changes of many different BP parameters.

The total pressure $P_{t,sup}$ (=static pressure + dynamic pressure) at the supply oil input is imposed as a boundary condition, to improve computational convergence. Thus, the static pressure (supply pressure) and flowrate (supply oil flow) at the supply oil inlet are calculated from the CFD simulation. Figures 13–15 show the effects of the main parameter changes on the axial MC distributions of Eqs. (3) and (4). Figures 13(*a*) and 13(*b*) illustrate the effect of

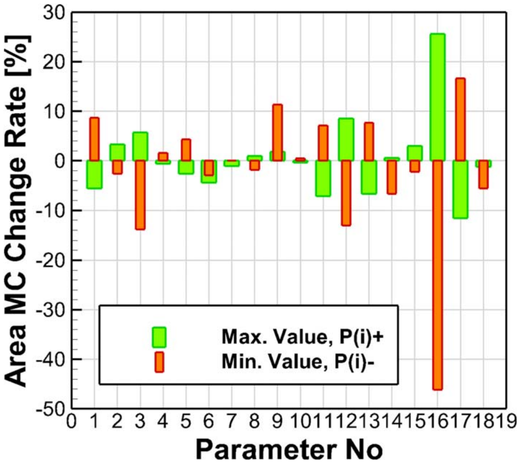

Fig. 12 Percent change in area MC of Eqs. (1) and (2), at the BP input parameter bounds in Table 4

changing the bearing width to radius ratio $P_{(3)}$ of Table 4 and Fig. 5. Reducing the ratio results in an increase in the nozzle effect region and end effect region, a decrease in the area MC (−13.8%) of Eq. (1), and increases in the supply pressure (+4.5%) and averaged shear stress (+11.5%) between pads.

Figures 14(*a*) and 14(*b*) illustrate the effect of changing the parameter $P_{(12)}$, the shaft surface speed in Fig. 5 and Table 4. Positive and negative values of $P_{(12)}$ cause increase and decrease, respectively, in the area MC of Eq. (1) and the axial MC of Eq. (3). The shear stress is significantly increased (+26.1%) at the higher speed in Fig. 14(*a*), which causes a significant increase in the between pad-drag torque (BP-drag torque) at higher speed. Figures 14(*c*) and 14(*d*) illustrate the effect of changing the parameter $P_{(13)}$, the total supply pressure in Fig. 5 and Table 4. The total supply pressure strongly influences the axial MC of Eq. (3) near the nozzle. The supply pressure (+37.4% at a high value) and shear stress (+6.7% at a high value) are proportional to the total supply pressure.

Figure 15 shows that the main operating parameters have a strong influence on the supply pressure, BP shear stress, and axial MC in all regions (nozzle effect region, uniform mixing region, and end

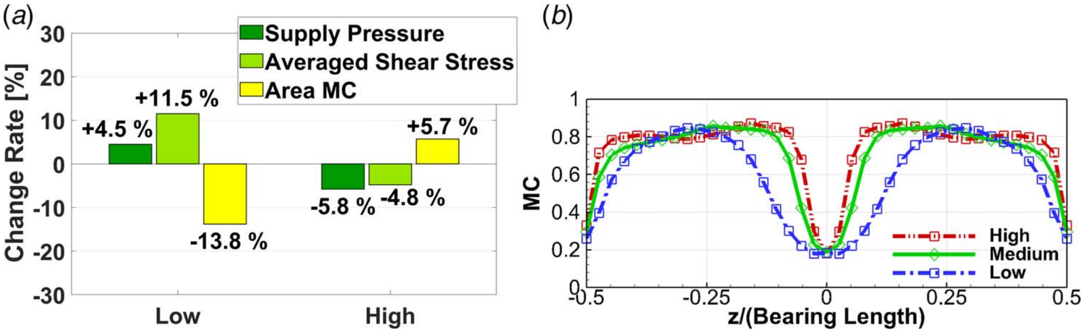

Fig. 13 MC, supply pressure, and averaged shear stress sensitivities to changes of a dominant geometric BP parameter (L_1/R_s) in Table 4: (*a*) change rate versus $P_{(3)} = L_1/R_s$ and (*b*) axial MC versus $P_{(3)} = L_1/R_s$

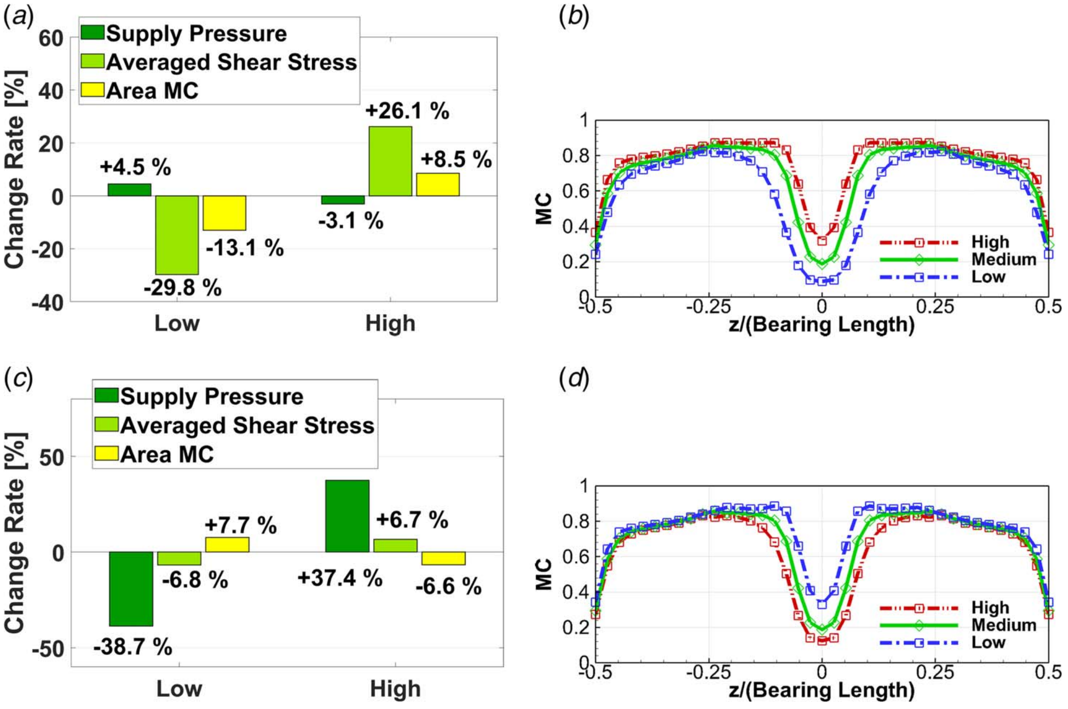

Fig. 14 MC, supply pressure, and averaged shear stress sensitivites to changes of dominant BP operating parameters (U_s, $P_{t,sup}$) in Table 4: (*a*) change rate versus $P_{(12)} = U_s$, (*b*) axial MC versus $P_{(12)} = U_s$, (*c*) change rate versus $P_{(13)} = P_{t,sup}$, and (*d*) axial MC versus $P_{(13)} = P_{t,sup}$

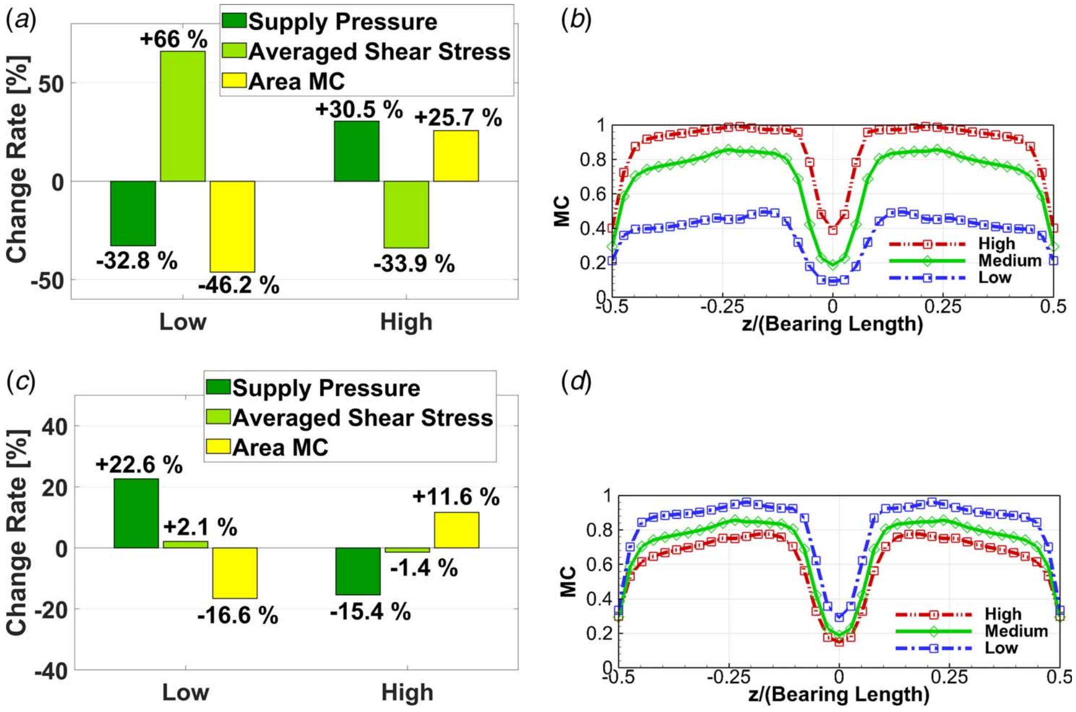

Fig. 15 MC, supply pressure, and averaged shear stress sensitivities to changes of dominant BP operating parameters ($h_{in}/C_{l,b}$, $h_{out}/C_{l,b}$) in Table 4: (*a*) change rate versus $P_{(16)} = h_{in}/C_{l,b}$, (*b*) axial MC versus $P_{(16)} = h_{in}/C_{l,b}$, (c) change rate versus $P_{(17)} = h_{out}/C_{l,b}$, and (*d*) axial MC versus $P_{(17)} = h_{out}/C_{l,b}$

effect region). The film thickness ratio at the BP inlet $P_{(16)} = h_{in}/C_{l,b}$ and at the BP outlet $P_{(17)} = h_{out}/C_{l,b}$ have the strongest influence. The BP in and out flowrates are proportional to the shaft surface speed, film thickness, and the gradient of the pressure at the leading and trailing edges. The film thickness strongly affects the BP inlet and outlet flowrates. Hence, the ratio of the BP inflow and outflow ($Ya = Q_{in}/Q_{out}$) plays an important role to determine the MC due to the significance of the parameters $P_{(16)}$ and $P_{(17)}$. Figures 15(*a*) and 15(*b*) show that increasing the BP inlet film thickness ratio $h_{in}/C_{l,b}$ will raise the BP inflow from the preceding pad, leading to higher MC because the advection heat of this BP inflow is dominant for determining the BP outflow temperature. Conversely higher advection heat from the supply oil will be transferred into the BP outflow, which will lower MC, if the film thickness is reduced at the BP inlet. The film thickness ratio $h_{out}/C_{l,b}$ at the BP outlet influences the BP outflow. Its increase will increase the influx of advection heat from the supply oil, leading to a reduction in MC, as shown in Figs. 15(*c*) and 15(*d*).

7.2 Regression Through Machine Learning-Artificial Neural Network

Table 5 lists the upper and lower bounds for the nine dominant input parameters selected for regression models through the parametric study. The bounds are based on review of bearing manufacturer catalog values, for example, bearing length ($P_{(3)}$) and radius ($P_{(6)}$). Bounds on operating parameters, such as journal speed ($P_{(12)}$) and total supply pressure ($P_{(13)}$) were selected in a similar manner. Maximum temperature ($P_{(9)}$) of the BP inflow was chosen based on the melting temperature of the pad babbitt surface. Bounds on the pressure parameters ($P_{(14)}$, $\overline{P}_{in}$) and ($P_{(15)}$, $\overline{P}_{out}$), and film thickness parameters ($P_{(16)}$,$h_{in}/C_{l,b}$) and ($P_{(17)}$, $h_{out}/C_{l,b}$), at the BP inlet and outlet, were selected based on maintaining a reasonable mass balance of the BP inflow and outflow. This was accomplished by examination of the Reynolds model predictions for various input conditions.

Table 5 Selected input parameters and the bounds

Parameter no.[a]	Min value, $P_{(i),\mathrm{Min}}$	Max value, $P_{(i),\mathrm{Max}}$	Unit
(3) L_1/R_s	0.4	1.0	–
(6) R_s	25.4	76.2	(mm)
(9) T_{in}	50	120	(°C)
(12) U_s	15	95	(m/s)
(13) $P_{t,sup}$	0.01	0.7	(MPag)
(14) $\overline{P}_{in}$	0	1.2	(MPag)
(15) $\overline{P}_{out}$	0	0.65	(MPag)
(16) $h_{in}/C_{l,b}$	0.3	2.2	–
(17) $h_{out}/C_{l,b}$	0.3	2.2	–

[a]The description of the parameter number index is represented in Table 2.

At this point, the ANN learning process with LMB and Bayesian regularization, as described in Sec. 5, is applied. Table 6 lists the three different DOE approaches that were tested. Design of experiment-A is the conventional full factorial with two levels, and the DOE-B and DOE-C are the proposed combination of full factorial and LHS in this study. The DOE-C method is the case which increases the LHS number from the DOE-B.

Figure 16 shows the SSE for the area-MC ANN according to the training epoch. The SSE is calculated based on transformed −1 ∼ +1 values of the output values. The SSE of all DOEs decreases

Table 6 Applied DOE method and number of data set

DOE case	DOE-A		DOE-B		DOE-C	
DOE type	FF	LHS	FF	LHS	FF	LHS
Training data set	512	0	512	512	512	1024
Test data set	219		438		658	
Total data set	731		1462		2194	

Note: FF: full factorial; and LHS: Latin hypercube sampling.

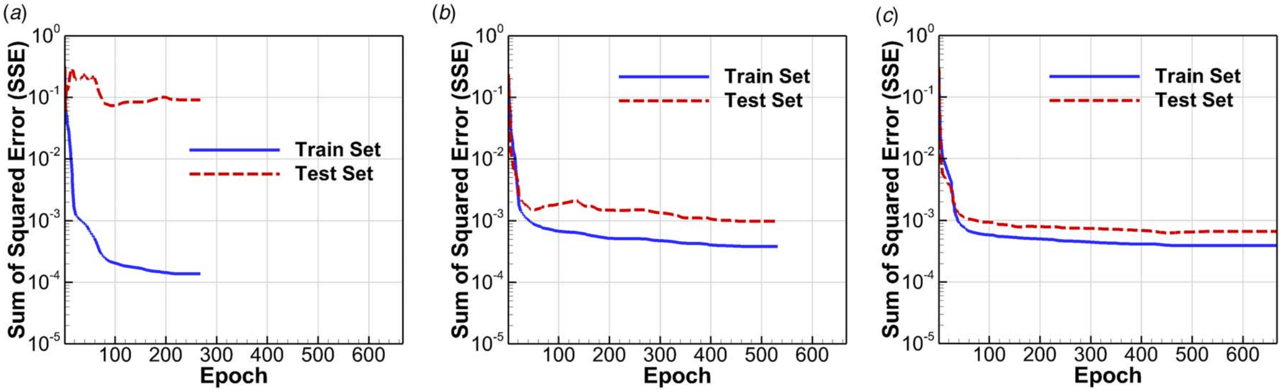

Fig. 16 SSE according to DOE type (20 neurons): (*a*) DOE-A, (*b*) DOE-B, and (*c*) DOE-C

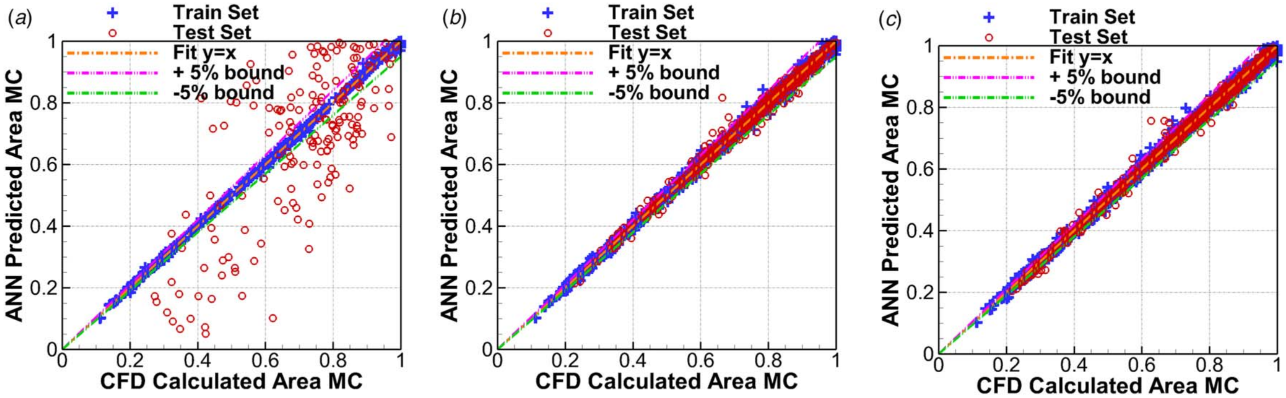

Fig. 17 Effect of DOE type (20 Neurons) on ANN performance for area MC (Eq. (1)): (*a*) DOE-A, (*b*) DOE-B, and (*c*) DOE-C

consistently well for the train set. However, the DOE-A method fails to obtain adaptable accuracy on the test set, which means that it could not achieve generalization. The poor performance of the DOE-A ANN is shown in Fig. 17(*a*).

Design of experiment-B and DOE-C exhibit strongly decreasing SSE for both the train and test data sets, as shown in Figs. 16(*b*) and 16(*c*). The DOE performance achieves generalization, as confirmed in Figs. 17(*b*) and 17(*c*). The combined DOE approach and LMB-Bayesian regularization show excellent performance. The test set error is reduced significantly from DOE-A to DOE-B by simply adding an equal number of the LHS as shown in Table 6. This is an advantage over the three-level full factorial method (Fig. 4(*a*)), which requires 19,683 samples for the training. There is a small improvement when adding the LHS train set, which is DOE-C, so the DOE-C method is chosen for the regression model.

Increasing the number of neurons reduces the error of the train set; however, too large of a number may cause excessive computational load to train and may fail generalization. Figure 18 shows the effect of the number of neurons on the ANN performance of the area-MC ANN model. The performance shows increasing improvement as the number of neurons increases from five to the optimal number 25. The optimal number of neurons is illustrated in Fig. 19(*a*) for the area MC of Eq. (1). The SSE of the regression models for BP-drag torque and supply flowrate and BP-pressure ANN (Sec. 6) are provided in Figs. 19(*b*) and 19(*c*), and the optimal number of

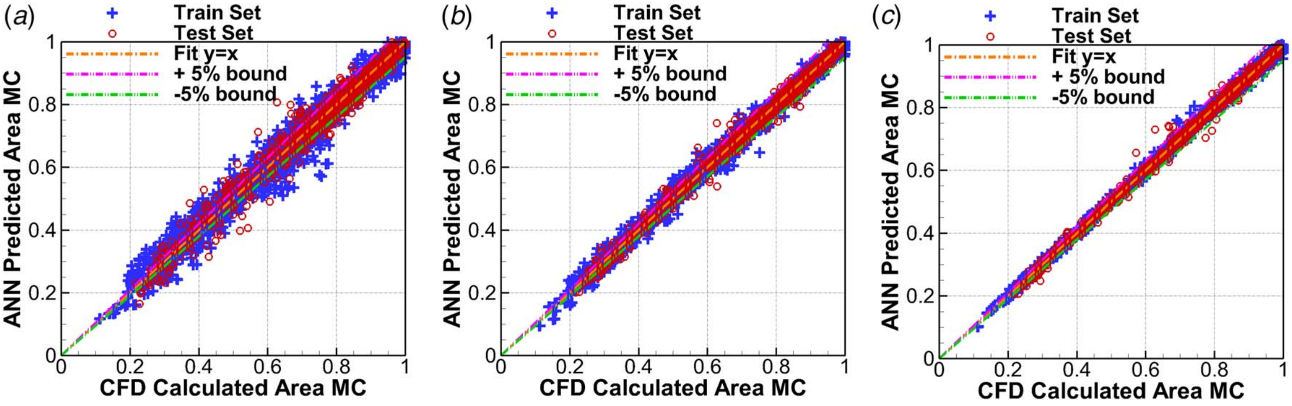

Fig. 18 Effect of the number of neurons (2194 data samples) on ANN performance for area MC (Eq. (1)): (*a*) 5 neurons, (*b*) 10 neurons, and (*c*) 25 neurons (optimal)

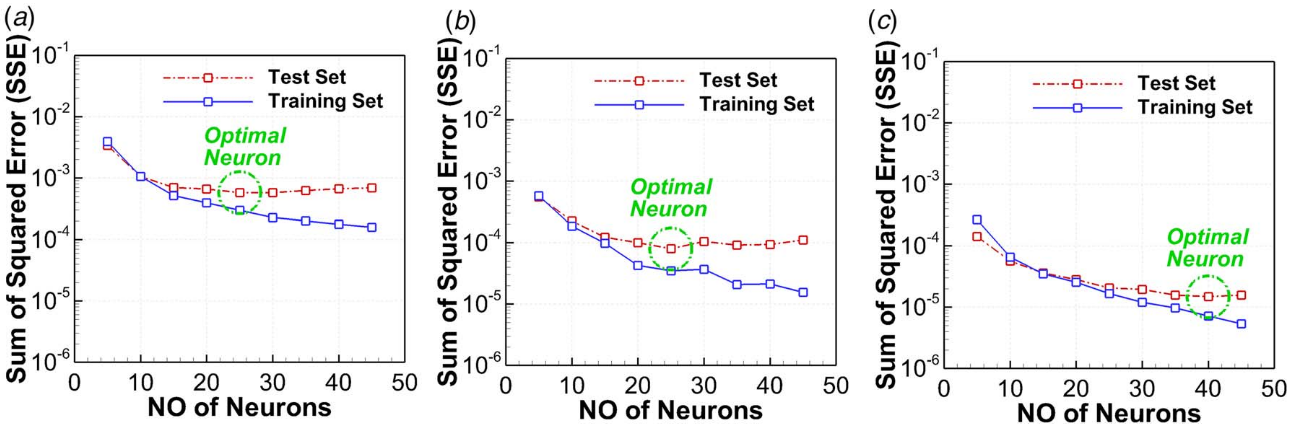

Fig. 19 Effect of the number of neurons (2194 data samples) on SSE: (*a*) area-MC ANN, (*b*) BP-drag torque and supply flowrate ANN, and (*c*) BP-pressure ANN

neurons is given in Table 7. These regression models and those for MC are utilized to improve the Reynolds model.

It is noted that the SSE of the test set does not improve or worsen over its optimal neuron number value, even though the SSE of the training set continuously decreases. So, utilization of more neurons than optimal values is not helpful for improving the regression model's accuracy.

The training procedure produced the final regression model using the optimal neuron numbers shown in Table 7. Its performance is illustrated in Fig. 20 for area-MC (Eq. (1)), BP-drag torque and supply flowrate, and BP-pressure ANN models. All ANN models show excellent performance. These ANN models are combined with the Reynolds model in Sec. 7.4 to overcome shortcomings of the conventional approach.

7.3 Regression Through Log Fitting of Non-Dimensional Parameter (*Ya*).

This section presents a log fitting method, utilizing the non-dimensional parameter (*Ya*) of Table 1, to yield a computationally simplified regression model for MC. This approach can be used as an alternative to the direct ANN model, although the accuracy is reduced. The non-dimensional parameter (*Ya*) is derived from the mass and heat balance in the BP. Then, the CFD results are fitted with a log function of *Ya*.

Figure 21 depicts all boundary flows between pads, and the corresponding mass balance equation is

$$\iint_{sup} \rho u dA + \iint_{in} \rho u dA - \iint_{out} \rho u dA - \iint_{side} \rho u dA = 0 \tag{33}$$

or expressed in terms of flowrate symbols becomes

$$Q_{sup} + Q_{in} - Q_{out} - Q_{side} = 0 \tag{34}$$

The energy balance between pads, neglecting heat convection and dissipation because of their minor effects, becomes

$$\iint_{sup} \rho u c_p T dA + \iint_{in} \rho u c_p T dA - \iint_{out} \rho u c_p T dA - \iint_{side} \rho u c_p T dA = 0 \tag{35}$$

Table 7 Optimal number of neurons

	Area-MC (Eq. (1))	BP-D.T. & S.F.R.	BP-pressure
No. of neurons	25	25	40

Note: D.T.: drag torque; and S.F.R.: supply flowrate.

This equation may be written assuming constant fluid specific heat (c_p) and density (ρ), and Eq. (2) as

$$Q_{sup}T_{sup} + Q_{in}\overline{T}_{in} - Q_{out}\overline{T}_{out} - Q_{side}\overline{T}_{side} = 0 \tag{36}$$

Combining Eqs. (34) and (36) and utilizing Eq. (1) yield

$$\frac{(\overline{T}_{out} - T_{sup})}{(\overline{T}_{in} - T_{sup})} = \frac{Q_{in}}{Q_{out}} - \frac{Q_{side}}{Q_{out}}\frac{(\overline{T}_{side} - T_{sup})}{(\overline{T}_{in} - T_{sup})} = \overline{MC} \tag{37}$$

This result shows that the area MC is a function of BP inflow, outflow, side flow, side temperature, inlet temperature, and supply oil temperature, i.e.

$$\overline{\mathrm{MC}} = f(Q_{in}, Q_{out}, Q_{side}, \overline{T}_{side}, \overline{T}_{in}, T_{sup}) \tag{38}$$

The middle expression in Eq. (37) is dominated by Q_{in}/Q_{out} because of the high-speed rotating shaft effect

$$\frac{Q_{in}}{Q_{out}} >> \frac{Q_{side}}{Q_{out}}\frac{(\overline{T}_{side} - T_{sup})}{(\overline{T}_{in} - T_{sup})} \tag{39}$$

This result supports using a regression model to provide MC as a function of Q_{in}/Q_{out} and to compensate for ignoring the right side term in Eq. (39). A log function is utilized for this purpose due to its simplicity and its high goodness of fit. Define

$$Ya \equiv \frac{Q_{in}}{Q_{out}} \tag{40}$$

The CFD results obtained from DOE-C in Sec. 7.2 are utilized for the regression by *Ya*. Figure 22(*a*) shows that the total data set has log function characteristics, and lies within ±15% bounds of the log fitting results, as shown in Fig. 22(*b*).

The mathematical expression for the log fit is

$$\overline{\mathrm{MC}} = \min\left[0.422 \ln(|Ya|) + 0.801,\ 1\right] \tag{41}$$

The performances of machine learning and log fitting are compared in Table 8. The MSE is the mean squared error defined by Eq. (42), and it is calculated based on the actual values. The *R*-squared is a frequently employed parameter for evaluating regression performance as defined in Eq. (43). An *R*-squared near one indicates good performance. The machine learning-ANN regression provides greater accuracy for the area MC (Eq. (1)); however, the simplicity of the log approach makes it appealing for ease of implementation in a Reynolds code

$$\mathrm{MSE} = \frac{1}{N_{tot}}\mathrm{SSE} \tag{42}$$

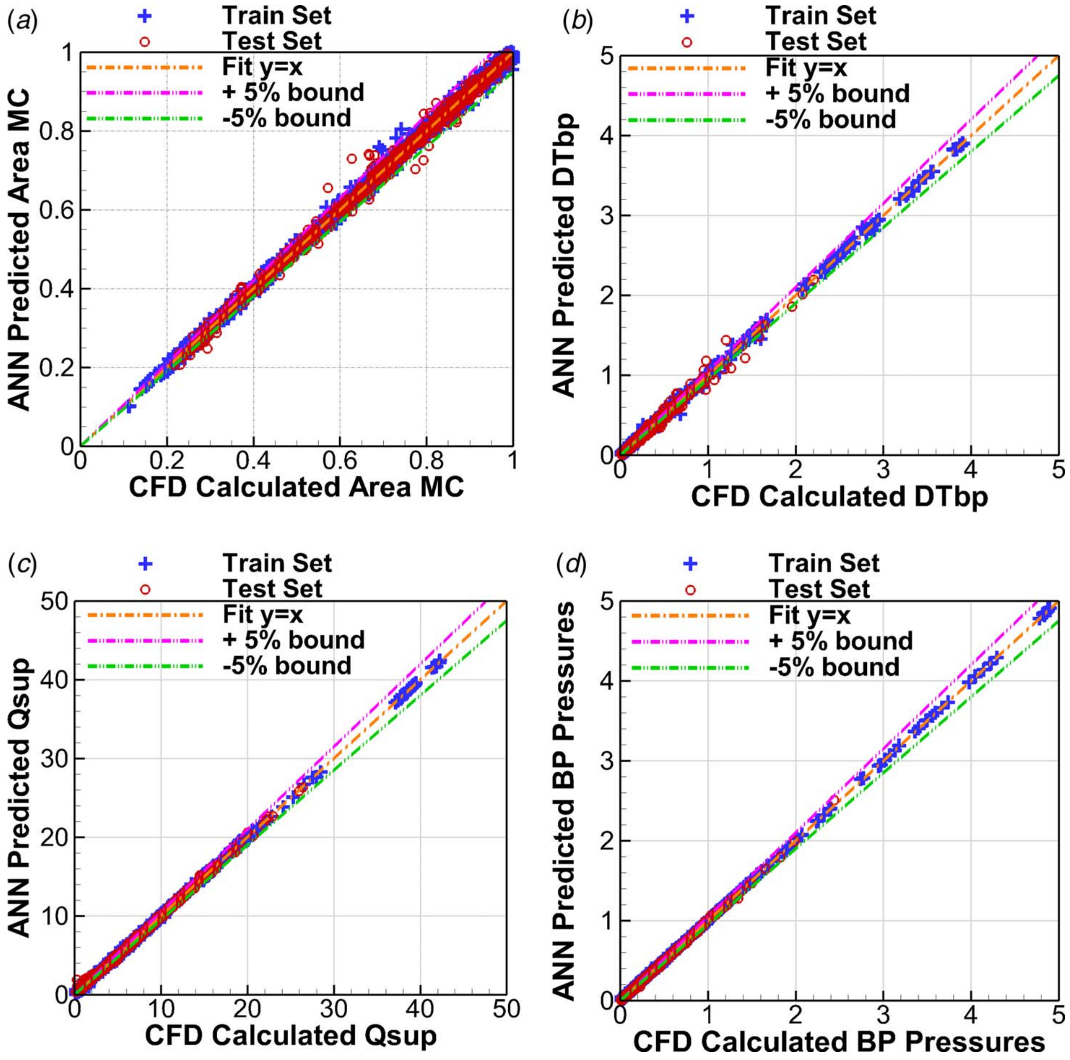

Fig. 20 Optimal regression results of machine learning (2194 data samples): (*a*) $\overline{MC}$ (Eq. (1)), (*b*) DT_{bp}, (*c*) Q_{sup}, and (*d*) BP pressures (P_{sup}, $\bar{P}_{in}$, $\bar{P}_{out}$)

$$R^2 = 1 - \frac{\text{SSE}}{\sum_{o=1}^{N_{tot}} (OUTC_o - \overline{OUT}_o)^2} \tag{43}$$

7.4 MLMC Reynolds Model Prediction Performance. The ANN models obtained from machine learning are combined with the Reynolds model, as described in Sec. 6, and the resulting modeling method is referred to as the MLMC Reynolds model. The log fit versus *Ya* is also combined with the Reynolds model, and the resulting modeling method is referred to as the log fit mixing coefficient (LFMC) Reynolds model. The results which follow compare predictions from the full CFD model, the conventional Reynolds approach with MC extremes (0.4, 1.0) [4], and the MLMC and LFMC Reynolds models. In all simulations, the area MC is applied to the Reynolds model. The input parameters for the model and further details of the physical modeling method are provided in the Part I paper.

Figures 23 and 24 show comparisons of the static model outputs, and Figs. 25 and 26 show comparisons of dynamic model outputs (stiffness and damping). Figure 23(*a*) shows that for eccentricity ratio versus rpm, the MLMC Reynolds model shows the best agreement with full CFD. Both MLMC and LFMC show good agreement with full CFD. The conventional fixed MC approach shows a potential for large errors. Figure 23(*b*) shows small absolute difference in attitude angle versus speed predictions between the various approaches and full CFD. Figure 23(*c*) shows small errors between the MLMC and full CFD predictions for drag torque versus rpm. The LFMC approach shows somewhat larger errors than MLMC, and the conventional constant MC approach shows a wide spread in error depending on the MC value selected. Figure 24(*a*) shows that the MLMC and LFMC Reynolds models

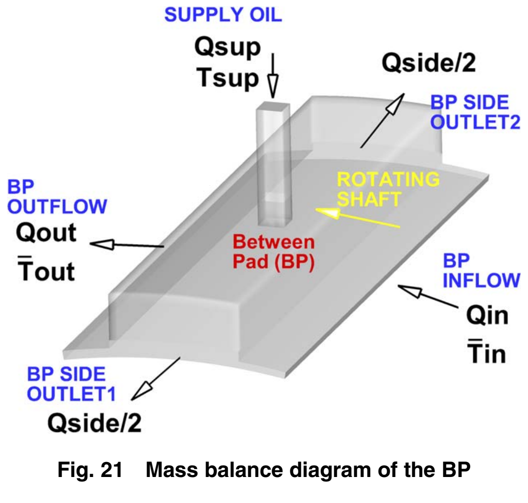

Fig. 21 Mass balance diagram of the BP

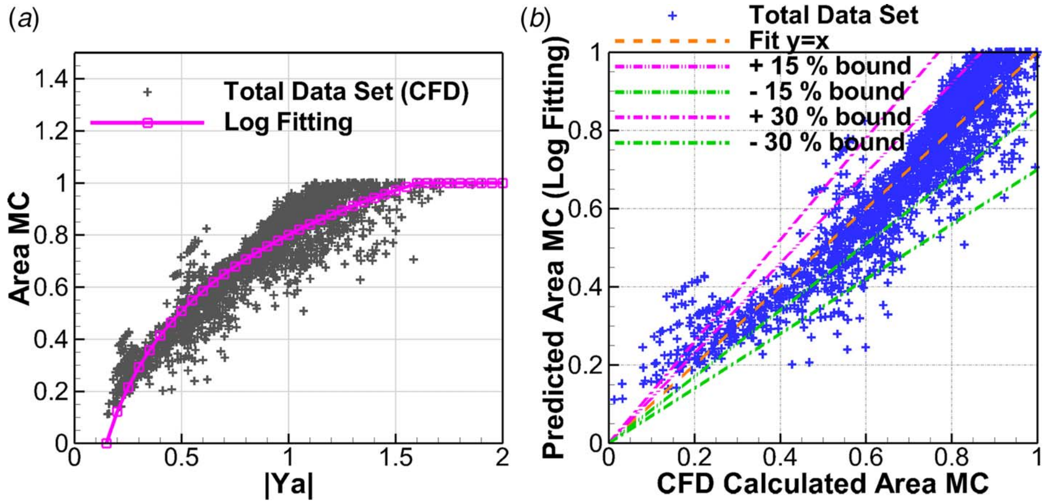

Fig. 22 Log fitting results (2194 data samples): (*a*) area MC ($\overline{\mathrm{MC}}$) versus || and (*b*) prediction performance by log fitting

over-predict the side leakage at operating speeds over 9000 rpm, but show very close agreement with CFD for the total supply flowrate. The conventional, constant assumed MC models cannot predict the supply flowrate.

Figures 24(*b*) and 24(*c*) show good agreement between the full CFD and MLMC and LFMC Reynolds models for predicting

Table 8 MSE and R^2 for the total data set

	Machine learning $\overline{\mathrm{MC}}$	Log fitting $\overline{\mathrm{MC}}$
MSE	1.3×10^{-4}	6.5×10^{-3}
R^2	1.0	0.87

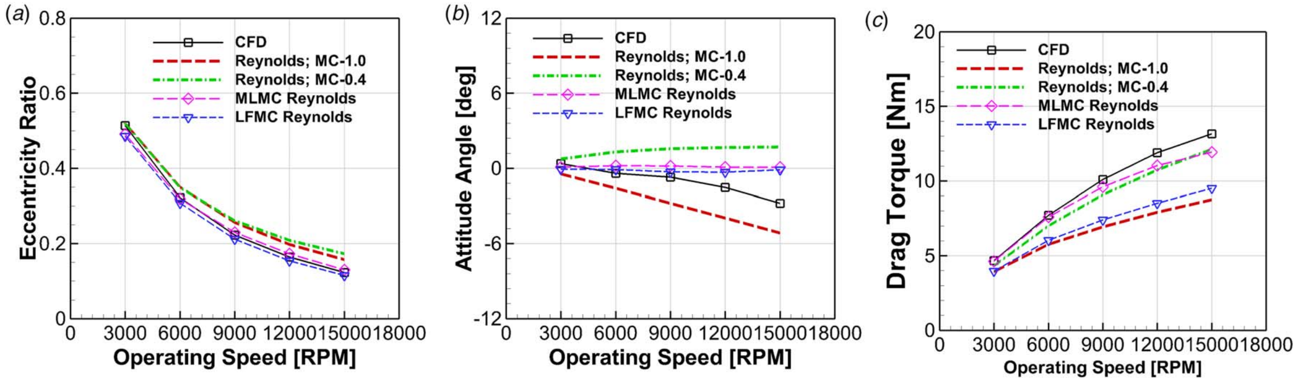

Fig. 23 Full CFD and conventional, MLMC and LFMC Reynolds model static results (TEHD analysis): (*a*) eccentricity ratio, (*b*) attitude angle, and (*c*) drag torque

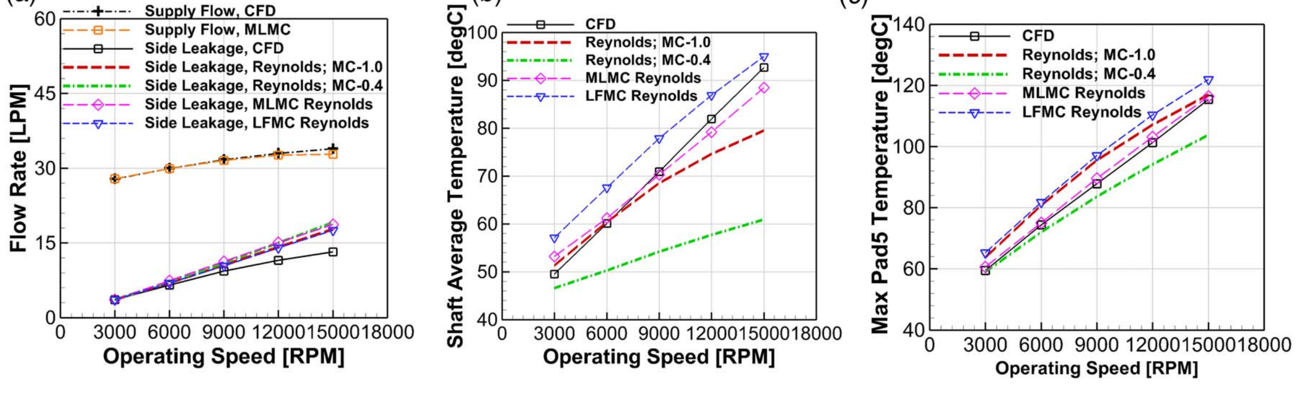

Fig. 24 Full CFD and conventional, MLMC and LFMC Reynolds model static results (TEHD analysis): (*a*) flowrate, (*b*) shaft average temperature, and (*c*) max pad5 temperature

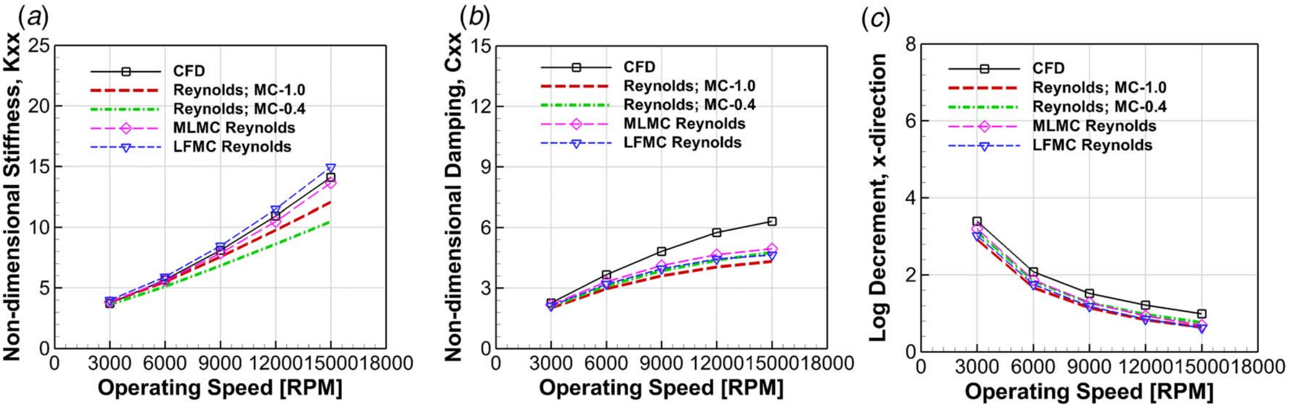

Fig. 25 Full CFD and conventional, MLMC and LFMC Reynolds model dynamic results (TEHD analysis): (*a*) direct stiffness Kxx, (*b*) direct damping Cxx, and (*c*) log decrement, *x*-direction

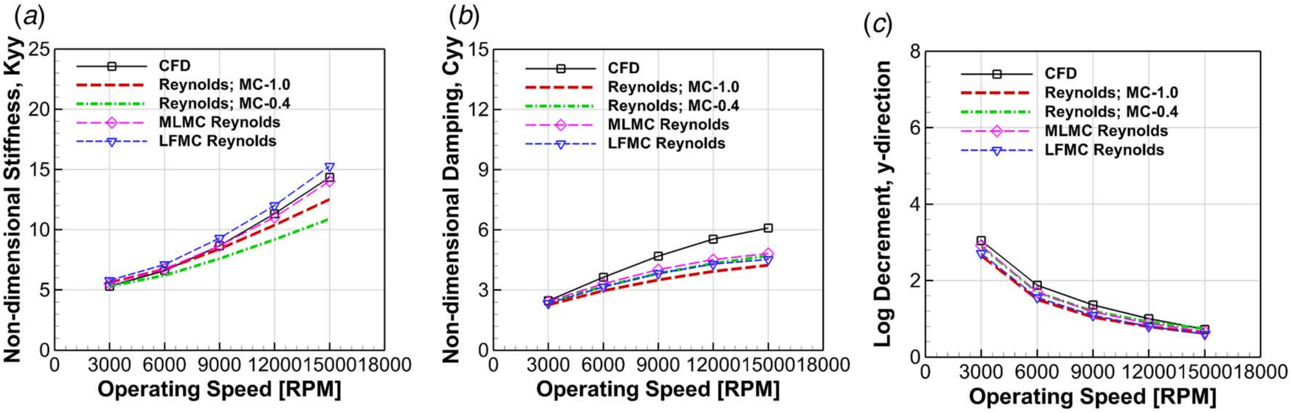

Fig. 26 Full CFD and conventional, MLMC and LFMC Reynolds model dynamic results (TEHD analysis): (*a*) direct stiffness Kyy, (*b*) direct damping Cyy, and (*c*) log decrement, *y*-direction

shaft and pad temperatures. The conventional, constant assumed MC model results show large variations in predicted temperatures depending on the MC selection, and the CFD results occur outside of the bounds from the MC-0.4 and MC-1.0 bounds in some instances.

Figures 25 and 26 show predictions of the non-dimensional dynamic coefficients that are frequency reduced at the synchronous speed frequency. Figures 25 and 26 correspond to the *x*- and *y*-direction dynamic coefficients, respectively. Figures 25(*a*) and 26(*a*) show that the MLMC and LFMC Reynolds direct stiffness predictions are excellent by comparison with the full CFD model. Figures 25(*b*) and 26(*b*) show non-negligible differences in direct damping, between the CFD and proposed Reynolds approaches. Sources of error compared with the full CFD approach stem from the use of a uniform MC in the Reynolds approaches, as opposed to a radially and axially varying MC at the pad inlet in the CFD approach. The log decrement predictions generally all agree well with CFD, as shown in Figs. 25(*c*) and 26(*c*). The Jeffcott rotor mass is 1019 kg for determining log decrements.

Figures 27(*b*) and 27(*c*) show area MC versus rpm plots determined by the MLMC approach, for different BP locations within the TPJB. It is notable that the MCs vary considerably versus BP locations, generally increase with rpm. The difference of MC depending on BP location can be explained by considering the parameter *Ya*, which from Eq. (40) $Ya = Q_{in}/Q_{out}$. The *Ya* is the ratio of the BP inflow and outflow, and the flows are quite proportional to the film thickness. Thus, the MC is approximately proportional to the film thickness ratio h_{in}/h_{out}, and it is expected that the ratio is higher in the BP3 and BP4 than the others concerning the film thickness model, so the higher MCs are predicted in the BPs.

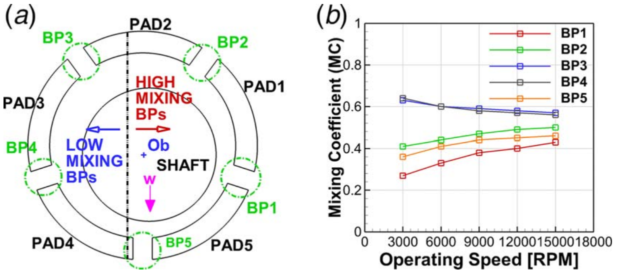

Fig. 27 Area MC versus BP location and RPM: (*a*) BP location illustration and (*b*) area MC; TEHD MLMC Reynolds

8 Conclusion

The Part I paper validated a novel TPJB TEHD-CFD modeling approach, including pad flexibility, by comparison of predictions with measured data. It also demonstrated that the accuracy of the conventional Reynolds modeling approach was questionable due to the uncertainty in guessing appropriate values for MCs. A novel approach for improving the Reynolds modeling results was developed utilizing an ANN machine learning regression for MCs, utilizing CFD to solve a myriad of TPJB configurations generated by DOE. The ranges of the DOE parameters were selected to reflect those commonly used in industrial applications. A preliminary study was performed of just the between pad BP region, which showed that the MC had a strong axial dependence resulting from the fresh oil flow through a nozzle. This study also revealed a very strong dependence of the MC on a large number of BP geometric and operating parameter values. This highlighted a need for an effective regression technique, such as machine learning. The number of input parameters was reduced to a smaller set of primary parameters that showed the largest effect on the MC. The input values of the training data samples were extracted from a novel DOE method. The DOE method consolidated the two-level full factorial and LHS approaches which led to significant improvements in accuracy and computation time reduction of the ANN machine learning.

Thermo-elasto-hydrodynamic CFD simulations were performed on the train data set obtained from the DOE and the test data set. The results provide output data to the ANN during the learning process. The ANN was trained, without an overfitting problem, utilizing the LMB with the Bayesian regularization. The MC, BP supply flowrate, drag torque, and pressures were regressed by ANN machine learning. These ANN models were directly integrated with the Reynolds TPJB model, to form the MLMC and LFMC Reynolds TPJB models. The former model utilizes the ANN machine learning regressions directly. The latter provides an easily implemented result for providing MC in the form of a log fit of MC versus the newly defined non-dimensional parameter $Ya = Q_{in}/Q_{out}$. Comparisons between the full CFD versus the MLMC Reynolds and LFMC-Reynolds bearing modeling approaches showed in general good agreement. Both MLMC Reynolds and LFMC-Reynolds approaches replace the conventional approach of guessing MC, which by Fig. 27 vary considerably, even on which pad is considered. The MC is instead derived from ANN machine learning based regressions of results obtained from DOE selected, very high fidelity CFD models.

The paper provides an "indirect" experimental validation of the MLMC approach. The present MLMC code was developed for a full leading edge geometry, without the leading edge groove (LEG) of the bearing in the experimental results (second example in Part I). Including the LEG would introduce additional parameters and increase the dimensions of the training set. Thus, the present code programmed the MLMC for a standard leading edge. In Part I, we presented the CFD simulations for two bearings with very similar geometry, loading, and speed.

- (First Bearing in Sec. 3, Part I): 101.6 mm diameter, 50.8 mm length, 0.0749 mm bearing clearance, conventional lubrication
- (Second Bearing in Sec. 4, Part I): 101.6 mm diameter, 60.3 mm length, 0.0814 mm bearing clearance, LEG lubrication

The validity of the CFD model was verified by comparison with the test results of the seond bearing (Kulhanek, 2010). It follows that since the

1. First and second bearing have very similar geometries.
2. Exactly identical governing equations and modeling techniques in the CFD model are applied for both bearing's simulations.
3. Identical mesh density is applied to first and second bearings.
4. Loads and rpm are very similar

it is reasonable to assume that the first bearing's CFD model was "indirectly" experimentally validated. Although not ideal, it is likewise reasonable to conclude that the validation of the MLMC-TEHD approach by considering bearing 1 in Part II provides an "indirect" experimental validation of the approach. That being said, we are presently updating the MLMC codes to include LEG and will perform the direct experimental validation with bearing 2 in the future. Part II also includes comparison of the MLMC approach with a full bearing CFD simulation which is in itself a convincing validation, given the higher fidelity and accuracy of the full bearing CFD model.

The approach presented provides a means to obtain improved models for TPJB static and dynamic analyses which benefit from the high accuracy of CFD models, while preserving the high computational efficiency of the Reynolds approach.

Acknowledgment

The authors appreciatively acknowledge the funding for this research from the Texas A&M Turbomachinery Research Consortium (TRC) and the Texas A&M High-Performance Research Computing Center (HPRC).

Conflict of Interest

There are no conflicts of interest.

Nomenclature

e = error
u = fluid velocity (m/s)
w = weighting factor
y = neuron's input
F = neuron's defined derivative function
P = pressure (Pa)
Q = flowrate (m^3/s)
S = neuron's slope
T = mass flow averaged temperature at line (°C)
X = neuron's net value
Y = neuron's net output
$\overline{P}$ = mean pressure (Pa)
$\overline{T}$ = mass flow averaged temperature at area (°C)
c_p = fluid specific heat (J/(kg K))
t_p = pad thickness (m)
$C_{l,b}$ = bearing clearance (m)
F_{cost} = cost function
$P_{t,sup}$ = total supply pressure (Pa)
$P_{(i)}$ = input parameter of i index
R_s = shaft radius (m)
T_{sup} = supply temperature (°C)
U_s = shaft speed (m/s)
$\overline{Q}_{sup}$ = standard supply flowrate (m^3/s)
DT = drag torque (Nm)
INP = input value
MC = axially varying mixing coefficient
$OUTC_o$ = desired output value
$OUTN_o$ = aritificial neural network output value
$\overline{\text{MC}}$ = axially averaged mixing coefficient
α = weight regularization parameter
β = error regularization parameter
γ = effective parameter
δ = neuron's defined delta
μ = combination coefficient
μ_f = fluid dynamic viscosity (Pa $\cdot$ s)
ρ = density (kg/m^3)
$\{e\}$ = error vector
$\{g\}$ = gradient vector
$\{w\}$ = weight vector
$[H]$ = Hessian matrix
$[J]$ = Jacobian matrix
$[\delta]$ = delta matrix

Superscript

$*$ = old value during iterative calculation

Subscripts

bp = between pads
in = BP inflow
out = BP outflow
op = on pad
$side$ = BP sideflow
sup = supply flow
trn = training data
w = shaft surface wall boundary

References

[1] Abdollahi, B., and San Andrés, L., 2018, "Improved Estimation of Bearing Pads' Inlet Temperature: A Model for Lubricant Mixing at Oil Feed Ports and Validation Against Test Data," ASME J. Tribol., **141**(3), p. 031703.

[2] Hagemann, T., and Schwarze, H., 2018, "A Model for Oil Flow and Fluid Temperature Inlet Mixing in Hydrodynamic Journal Bearings," ASME J. Tribol., **141**(2), p. 021701.

[3] Hagemann, T., and Schwarze, H., 2019, "Theoretical and Experimental Analyses of Directly Lubricated Tilting-Pad Journal Bearings With Leading Edge Groove," ASME J. Eng. Gas Turbines Power, **141**(5), p. 051010.

[4] Yang, J., and Palazzolo, A., 2019, "3D Thermo-Elasto-Hydrodynamic CFD Model of a Tilting Pad Journal Bearing—Part I: Static Response," ASME J. Tribol., **141**(6), p. 061702.

[5] Yang, J., and Palazzolo, A., 2019, "3D Thermo-Elasto-Hydrodynamic CFD Model of a Tilting Pad Journal Bearing—Part II: Dynamic Response," ASME J. Tribol., **141**(6), p. 061703.

[6] Ettles, C., 1969, "Hot Oil Carry-Over in Thrust Bearings," Proc. Inst. Mech. Eng., Conf. Proc., **184**(12), pp. 75–81.

[7] Ettles, C. M. M., 1980, "The Analysis and Performance of Pivoted Pad Journal Bearings Considering Thermal and Elastic Effects," ASME J. Lubr. Tech., **102**(2), pp. 182–191.

[8] Mitsui, J., Hori, H., and Tanaka, M., 1983, "Thermohydrodynamic Analysis of Cooling Effect of Supply Oil in Circular Journal Bearing," ASME J. Lubr. Tech., **105**(3), pp. 414–420.

[9] Knight, J. D., and Barrett, L. E., 1988, "Analysis of Tilting-Pad Journal Bearing With Heat Transfer Effects," ASME J. Tribol., **110**(1), pp. 128–133.

[10] Brugier, D., and Pascal, M. T., 1989, "Influence of Elastic Deformations of Turbo-Generator Tilting Pad Bearings on the Static Behavior and on the Dynamic Coefficients in Different Designs," ASME J. Tribol., **111**(2), pp. 364–371.

[11] Taniguchi, S., Makino, T., Takeshita, K., and Ichimura, T., 1990, "A Thermohydrodynamic Analysis of Large Tilting-Pad Journal Bearing in Laminar and Turbulent Flow Regimes With Mixing," ASME J. Tribol., **112**(3), pp. 542–550.

[12] Kim, J., Palazzolo, A. B., and Gadangi, R. K., 1994, "TEHD Analysis for Tilting-Pad Journal Bearings Using Upwind Finite Element Method," Tribo. Trans., **37**(4), pp. 771–783.

[13] Kim, J., Palazzolo, A., and Gadangi, R., 1995, "Dynamic Characteristics of TEHD Tilt Pad Journal Bearing Simulation Including Multiple Mode Pad Flexibility Model," ASME J. Vib. Acoust., **117**(1), pp. 123–135.

[14] Lee, D., Sun, K., Kim, B., and Kang, D., 2017, "Thermal Behavior of a Worn Tilting Pad Journal Bearing: Thermohydrodynamic Analysis and Pad Temperature Measurement," Tribo. Trans., **61**(6), pp. 1074–1083.

[15] San Andrés, L., and Li, Y., 2015, "Effect of Pad Flexibility on the Performance of Tilting Pad Journal Bearings—Benchmarking a Predictive Model," ASME J. Eng. Gas Turbines Power, **137**(12), p. 122503.

[16] San Andrés, L., Tao, Y., and Li, Y., 2014, "Tilting Pad Journal Bearings: On Bridging the Hot Gap Between Experimental Results and Model Predictions," ASME J. Eng. Gas Turbines Power, **137**(2), p. 022505.

[17] Mehdi, S. M., Jang, K., and Kim, T., 2018, "Effects of Pivot Design on Performance of Tilting Pad Journal Bearings," Tribol. Int., **119**, pp. 175–189.

[18] da Silva, H. A. P., and Nicoletti, R., 2019, "Design of Tilting-Pad Journal Bearings Considering Bearing Clearance Uncertainty and Reliability Analysis," ASME J. Tribol., **141**(1), p. 011703.

[19] Suh, J., and Palazzolo, A., 2015, "Three-Dimensional Dynamic Model of TEHD Tilting-Pad Journal Bearing—Part I: Theoretical Modeling," ASME J. Tribol., **137**(4), p. 041704.

[20] Tong, X., and Palazzolo, A., 2018, "Tilting Pad Gas Bearing Induced Thermal Bow-Rotor Instability," Tribol. Int., **121**, pp. 269–279.

[21] Tong, X., and Palazzolo, A., 2017, "Measurement and Prediction of the Journal Circumferential Temperature Distribution for the Rotordynamic Morton Effect," ASME J. Tribol., **140**(3), p. 031702.

[22] Arihara, H., Kameyama, Y., Baba, Y., and San Andés, L., 2018, "A Thermoelastohydrodynamic Analysis for the Static Performance of High-Speed—Heavy Load Tilting-Pad Journal Bearing Operating in the Turbulent Flow Regime and Comparisons to Test Data," ASME J. Eng. Gas Turbines Power, **141**(2), p. 021023.

[23] Pinkus, O., 1990, *Thermal Aspects of Fluid Film Tribology*, ASME Press, New York, 187–197.

[24] Hagan, M. T., Demith, H. T., Beale, M. H., and Jesus, O. D., 2014, *Neural Network Design*, PWS Publishing Co., Boston, MA.

[25] Kaya, M., and Hajimirza, S., 2018, "Surrogate Based Modeling and Optimization of Plasmonic Thin Film Organic Solar Cells," Int. J. Heat Mass Transfer, **118**, pp. 1128–1142.

[26] Chopra, S., Yadav, D., and Chopra, A. N., 2019, "Artificial Neural Networks Based Indian Stock Market Price Prediction: Before and After Demonetization," J. Swarm Intel. Evol. Comput., **8**(1), p. 1000174.

[27] Pijanowski, B. C., Tayyebi, A., Doucette, J., Pekin, B. K., Braun, D., and Plourde, J., 2014, "A Big Data Urban Growth Simulation at a National Scale: Configuring the GIS and Neural Network Based Land Transformation Model to Run in a High Performance Computing (HPC) Environment," Environ. Model. Softw., **51**, pp. 250–268.

[28] Ramirez, C. A. P., Sanchez, J. P. A., Rodriguez, M. V., Adeli, H., Gonzalez, A. D., and Troncoso, R. J. R., 2019, "Recurrent Neural Network Model With Bayesian Training and Mutual Information for Response Prediction of Large Buildings," Eng. Struct., **178**, pp. 603–615.

[29] Fakhri, M., and Dezfoulian, R. S., 2019, "Pavement Structural Evaluation Based on Roughness and Surface Distress Survey Using Neural Network Model," Constr. Build. Mater., **204**, pp. 768–780.

[30] Hasan, S., 2019, "Prediction of Breast Cancer Type Based on Artificial Intelligence Technique," Int. J. Adv. Sci. Res. Eng., **5**(1), pp. 43–50.

[31] García-Alba, J., Bárcena, J. F., Ugarteburu, C., and García, A., 2019, "Artificial Neural Network as Emulators of Process-Based Models to Analyze Bathing Water Quality in Estuaries," Water Res., **150**, pp. 283–295.

[32] Levenberg, K., 1944, "A Method for the Solution of Certain Non-Linear Problems in Least Squares," Quart. Appl. Math., **2**(2), pp. 164–168.

[33] Marquardt, D. W., 1963, "An Algorithm for Least Squares Estimation of Nonlinear Parameters," SIAM J. Appl. Math., **11**(2), pp. 431–441.

[34] Hagan, M. T., and Menhaj, M. B., 1994, "Training Feedforward Networks With the Marquardt Algorithm," IEEE Trans. Neural Netw., **5**(6), pp. 989–993.

[35] Foresee, F. D., and Hagan, M. T., 1997, "Gauss-Newton Approximation to Bayesian Learning," Proceedings of International Joint Conference on Neural Networks,, Houston, TX, June 12, pp. 1930–1935.

[36] McKay, M. D., Beckman, R. J., and Conover, W. J., 1979, "A Comparison of Three Methods for Selecting Values of Input Variables in the Analysis of Output From a Computer Code," Technometrics, **42**(1), pp. 55–61.

[37] Queipo, N. V., Haftka, R. T., Shyy, W., Goel, T., Vaidayanathan, R., and Tucker, K., 2005, "Surrogate-Based Analysis and Optimization," Prog. Aerospace Sci., **41**(1), pp. 1–28.

[38] Nguyen, D., and Widrow, B., 1990, "Improving the Learning Speed of 2-Layer Neural Networks by Choosing Initial Value of the Adaptive Weights," Int. Joint Conf. Neural Netw., **3**, pp. 21–26.